



**HAL**  
open science

## Weather regimes and orographic circulation around New Caledonia

Jérôme Lefèvre, Patrick Marchesiello, Nicolas C. Jourdain, Christophe E. Menkès, Anne Leroy

► **To cite this version:**

Jérôme Lefèvre, Patrick Marchesiello, Nicolas C. Jourdain, Christophe E. Menkès, Anne Leroy. Weather regimes and orographic circulation around New Caledonia. *Marine Pollution Bulletin*, 2010, 61 (7-12), pp.413-431. 10.1016/j.marpolbul.2010.06.012 . hal-00765751

**HAL Id: hal-00765751**

**<https://hal.science/hal-00765751v1>**

Submitted on 18 Jan 2023

**HAL** is a multi-disciplinary open access archive for the deposit and dissemination of scientific research documents, whether they are published or not. The documents may come from teaching and research institutions in France or abroad, or from public or private research centers.

L'archive ouverte pluridisciplinaire **HAL**, est destinée au dépôt et à la diffusion de documents scientifiques de niveau recherche, publiés ou non, émanant des établissements d'enseignement et de recherche français ou étrangers, des laboratoires publics ou privés.

# Weather regimes and orographic circulation around New Caledonia

Jérôme Lefèvre<sup>a,\*</sup>, Patrick Marchesiello<sup>a</sup>, Nicolas C. Jourdain<sup>a</sup>, Christophe Menkes<sup>a</sup>, Anne Leroy<sup>b</sup>

<sup>a</sup>IRD, Noumea Centre, BP A5, 98848 Noumea cedex, New Caledonia

<sup>b</sup>Météo-France, Nouméa, New Caledonia

The local climate and island-scale circulation around New Caledonia is investigated using a 4-km resolution mesoscale atmospheric model in concert with QuikSCAT scatterometer winds at 12.5-km resolution. The mesoscale atmospheric weather regimes are first examined through an objective classification applied to the remote sensed winds for nine warm seasons from 1999 to 2008. Four main weather types are identified. Their corresponding synoptic-scale circulation reveals that they are strongly discernable through the position and intensity of the South Pacific Convergence zone (SPCZ), the mid-latitude systems, and the subtropical jet stream. The link between the mesoscale weather types and the two dominant large-scale modes of variability, namely the Madden–Julian Oscillation (MJO) and the El Niño–Southern Oscillation (ENSO), is also described in terms of their influence on the occurrence of each weather type. It shows that their occurrence is significantly controlled by both MJO and ENSO, through modulation of the SPCZ. The large-scale modes of variability are scaled down to island-scale circulation through synoptic and mesoscale regimes, and are eventually modulated by orographic and thermal control. The island-scale circulation is inferred in this study by applying the compositing method to both observed and simulated winds. Their comparison clearly shows the ability of the mesoscale model to capture the local circulation and its spatial and temporal variability. A scaling analysis conducted from the simulated atmospheric parameters shows that the mountain range of New Caledonia is hydrodynamically steep. As a result of trade-wind obstruction by the mountainous island, the flow is shaped by coastally trapped mesoscale responses, i.e., blocking, flow splitting and corner winds, with a spatial scale of about 150 km. Two main obstacles, Mont Panié and Mont Humboldt play a significant role on the dynamical behavior of the low-level flow, while the diurnal heating cycle in the vicinity of the Mainland strongly modulates the local circulation. Moreover, nocturnal drainage flow of cold air occurs on the leeward slope of Mont Humboldt and inhibits vertical mixing over the ocean, which results in a deceleration of surface winds.

## 1. Introduction

In the study of marine coastal phenomena involving biogeochemical cycles that depend on land inputs, ocean interaction, and local hydrodynamics, it is increasingly crucial that spatial and temporal details of surface forcing be accessible (Ouillon et al., 2010). By its geographical position, New Caledonia is under the influence of the trade-winds and a number of intra-seasonal to inter-annual large-scale modes of variability. These modes are scaled down to island-scale circulation through synoptic and mesoscale regimes eventually modulated by orographic and thermal control. Because accurate island-scale wind prediction requires knowledge of the local responses to a given synoptic scenario (Davidson et al., 1992), a study of synoptic and large-scale conditions is needed to accurately approach the downscaling prob-

lem. On the intra-seasonal timescale, the region is influenced by the Madden–Julian Oscillation (MJO, Madden and Julian, 1994), which is the strongest existing mode of tropical intra-seasonal atmospheric variability with its 30- to 80-day period. To date, only one study has described how the MJO may influence New Caledonia’s climate, using relatively coarse ERA40 Sea Level Pressure (Leroy, 2006). On inter-annual timescales, New Caledonia is impacted by El Niño–Southern Oscillation (ENSO). Delcroix and Lenormand (1997), using the low-resolution  $2^\circ \times 2^\circ$  Florida State University wind dataset, report significantly stronger southwesterly wind stress anomalies during El Niño and stronger north-easterlies during La Niña events. However, due to data limitation, they did not investigate New Caledonia’s mesoscale weather patterns. In the present study, a high-resolution classification of regional weather types and their connection with large-scale variability will provide insights on the link between both MJO and ENSO signals and New Caledonia’s weather. It will appear that the island-scale circulation is downscaled through orographic

\* Corresponding author. Tel.: +687 260 712; fax: +687 264 326.  
E-mail address: jlefevre@noumea.ird.fr (J. Lefèvre).

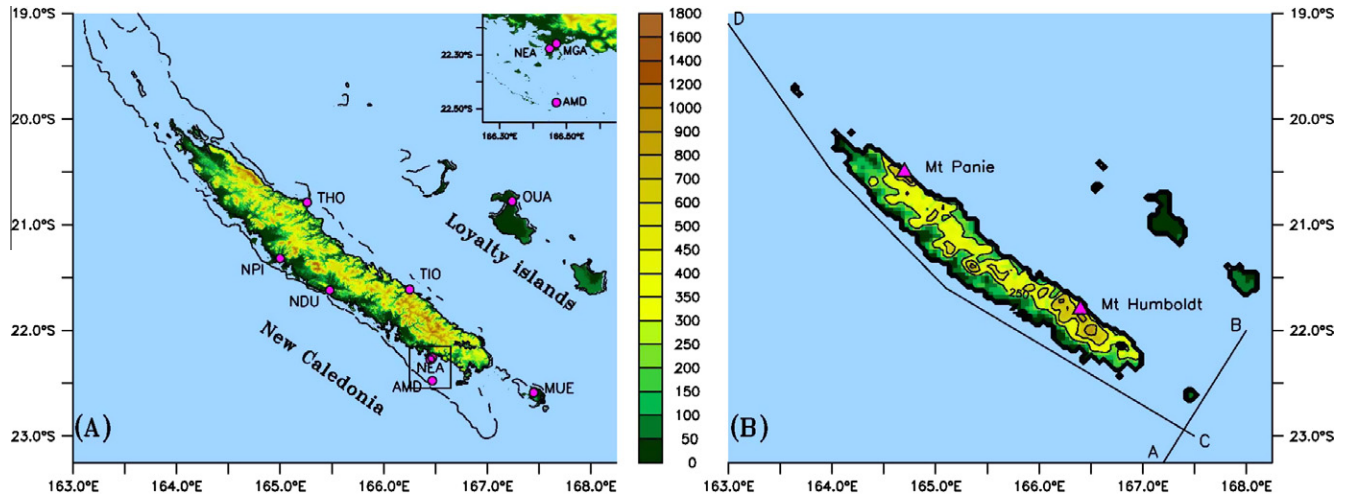


**Fig. 1.** Left: geography of New Caledonia, Mainland and dependencies. The locations of weather stations used for model validation are depicted. (NPI) Nepoui; (NDU) Nessadiou; (AMD) Amedee LightHouse; (OUA) Ouanaham airfield, Lifou island; (MUE) Moue airfield, Isle of Pins; (TIO) Thio; (THO) Touhu airfield; (NEA) Noumea, Major City; (MAG) Magenta airfield. Right: topography of the innermost 4-km-resolution domain (contour intervals = 250 m). The two main ridges are labeled. The lines AB and CD show, respectively, the vertical cross section used to assign value for the geophysical scaling and the along shore section on which the model simulation is displayed.

control of four prevalent weather types whose occurrences are controlled by these large-scale signals.

New Caledonia is made up of the Mainland, the Loyalty Islands, Isle of Pines and the Belep archipelago (Fig. 1). The Mainland is an elongated mountainous island oriented in the south-easterly trade-wind axis and is roughly 50 km wide and 400 km long, surrounded by a shallow lagoon. Its topography is characterized by the Central mountain range, with a mean altitude of about 800 m. The mountainous relief stands closer to the east coast than the west coast. The highest peaks are located on the steeper eastern side, with Mont Panié (1628 m) in the north and Mont Humboldt (1618 m) in the south. They form the two main obstacles to the trade-wind flow and are below the trade-wind inversion (2.5–3 km; Fig. 2). The Mainland mountain range is irregular, interspersed with East–West valleys that form wide gaps. In comparison, the Loyalty Islands, Isle of Pines, and Belep are low-lying islands, with height below 150 m. The mountain range of New Caledonia is expected to have a significant impact on the regional circulation. Many studies have dealt with the local dynamical response of an isolated mountain range to an upstream airflow (Bauer et al., 2000; Petersen et al., 2005) and its consequences for the local climate of mountainous islands (Yang and Chen, 2008). Low-level airflow impinging on a mountain range can experience upstream blocking on the windward slope due to the piling up of heavy air, wave breaking aloft, flow splitting and lee vortices formation. These effects depend on the mountain shape, and characteristics of the ambient upstream air (Smith, 1989). Hills with a short horizontal length scale (from a few hundred meters to a few kilometers) are only responsible for increased turbulence in the boundary layer, whereas mountain wave generation, low-level flow blocking and wake generation are expected for larger features (Vosper and Brown, 2007). According to its regime flow parameters (i.e., vertical stability, moisture content, flow speed and direction), the mountainous island of New Caledonia may lead to blocked and unblocked flow regimes, which may dictate precipitation amounts and distribution (Lin et al., 2001; Chen and Lin, 2005). In addition to island blocking and orographic lifting, land–sea thermal forcing can also be affected by orography, due to differential solar heating of the valley slopes, modulated by orographic clouds, adding up to land–sea breeze effects (Yang and Chen, 2008). In this study, preliminary results on the spatial structure of the trade-wind flow impinging on the New Caledonia mountain range are investigated with the use of a mesoscale numerical model combined with high-

resolution remote sensed sea surface winds from QuikSCAT. Since coastal winds are essentially a local, downscaled response to a given synoptic scenario, we examine the island-scale circulation associated with the most influential and prevalent weather regime, composed of nearly steady and persistent south-easterly trade winds during austral summer (November to April).

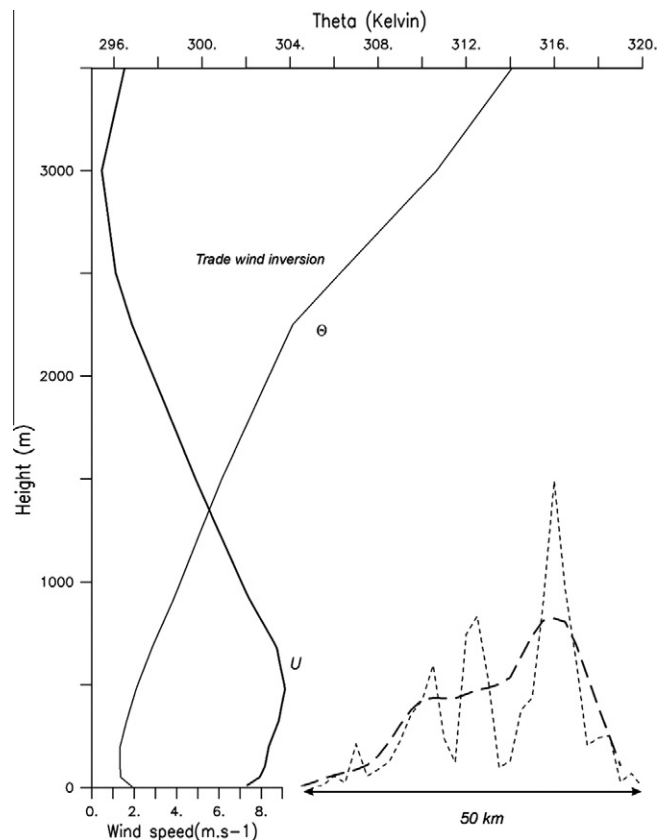


**Fig. 2.** Model mean vertical sounding at the upstream cross-wind section AB (Fig. 1): potential temperature (light line; units: Kelvin), and wind speed (thick line;  $m s^{-1}$ ). The light dashed line is a cross section (with an undefined abscissa) of Mt. Humboldt from the 50 m-resolution original elevation data; the thick dashed line shows the same cross section but for the smoothed model elevation.

The specific objectives of this study are (1) to isolate the observed dominant mesoscale circulation regimes and show their relation to the large-scale atmospheric circulation, (2) to examine the spatial structure and temporal variability of mesoscale circulation using both observations and a mesoscale model, (3) to explore thermal and orographic influences on the island-scale circulation associated with the SE trade-wind regime using scaling analysis (based on idealized studies) and statistical analysis of the model solution. The numerical model and datasets used in this study are described in Section 2 with the classification method to identify the dominant regimes of mesoscale circulation. In Section 3, those regimes are examined and connections to the intra-seasonal and inter-annual variability are made. The island-scale circulation produced by diurnal forcing and orographic effects is analyzed for the strong trade-wind regime in Section 4. Summary and conclusions are drawn in Section 5.

## 2. Data and model description

### 2.1. Model description and initialization

The atmospheric model used in our experiment is the Weather Research and Forecast model (WRF; Skamarock et al., 2005) with the ARW (Advanced Research WRF) dynamical solver. WRF integrates the fully compressible non-hydrostatic Euler equations; those equations are formulated using terrain-following mass vertical coordinate. The physical parametrizations include the WRF Single Moment 3-class Microphysics scheme (WSM3; Hong et al., 2004), Rapid Radiation Transfer Model longwave radiation (RRTM; Mlawer et al., 1997), a simple cloud-interactive short-wave radiation scheme (Dudhia, 1989), the Monin-Obukhov surface layer parameterization with Yonsei University (YSU) Planetary Boundary layer (Noh et al., 2003), Betts-Miller-Janjic cumulus parameterization (Janjic, 1994), and the Noah land-surface model which is a state-of-the-art 4-layer soil temperature and moisture model (see Xi, 2007, for a complete description). The topography of the model is interpolated and smoothed using a volume-conserving algorithm (Liang et al., 2005a). This treatment of topography allows us to properly represent lift forces perpendicular to the flow (Lott and Miller, 1997); it does not include a complementary blocked-layer drag parametrization (Kim and Doyle, 2005), but the resolution used here is sufficient to explicitly simulate the blocking process. Finally, subgrid-scale orographic effects are not parameterized in this model version, but we are aware that its effect on both form drag and radiation may be significant for mesoscale and synoptic modeling (Liang et al., 2005b).

WRF configuration uses 2-level, 2-way nested domains spanning the area of New Caledonia's Exclusive Economic Zone (20 km resolution) with refinement of the horizontal resolution over the Mainland of New Caledonia and its dependencies (4 km). The model grid has a vertical resolution of 30 levels. Terrestrial data (land use, soil type, annual deep soil temperature, monthly vegetation fraction, monthly albedo, and slope data) are provided by the US Geological Survey, apart from the 50 m topography of New Caledonia, which is provided by New Caledonia Remote Sensing and Geomatics Service (DTSI). The elevation data for the innermost grid is given in Fig. 1 along with the 50-m resolution original elevation map. A side effect of the orography smoothing is a reduction of high peaks and filling of the valleys. As an illustration, Fig. 2 shows a comparison between the original elevation and the model elevation for a vertical section across Mont Humboldt. The main topographic features and the mountain range aspect are well represented, but the 4-km grid resolution is unable to resolve the orography variance below 20 km.

The meteorological data used for model initialization and boundary conditions (pre-processed with the WPS package) are the 6 hourly NCEP operational analyses (NCEP-FNL, <http://nomad1.ncep.noaa.gov:9090/dods/gdas>). It includes the optimal interpolation (OI) sea surface temperature (SST) analysis produced weekly on a one-degree grid (Reynolds and Smith, 1994). Narrow and transient coastal SST fronts such as those induced by upwelling events (Marchesiello et al., 2010) are missing in this data and thus have no impact on the simulated atmospheric circulation presented in this study.

The time period of the simulation extends from 1-November-2005 00:00 to 30-April-2008 18:00 UTC and each year, only the summer months from November to April are computed. Initialization time is set to 10 days before November 1st, which are not considered in our analysis (spinup time). The model output was archived at hourly intervals, accounting for the 11-h time lag between New Caledonia's time-zone and UTC. Above the sea, the 10-m neutral equivalent wind ( $U_{10n}$ ) is estimated by the relation  $U_{10n} = U_* \sqrt{C_D}$ , with  $U_*$  the surface friction velocity computed by the surface-layer model and  $C_D$  the nonlinear drag coefficient, function of the 10-m wind field ( $U_{10}$ ), based on Trenberth et al. (1990).

### 2.2. High-resolution remote sensed surface wind: QSCAT QHR12

QuikSCAT data are invaluable in providing high-resolution wind fields, and numerous studies applied in open and coastal area point out its value to retrieve small-scale wind structures, air-sea interaction signatures and orographic circulation (Milliff et al., 2004; Chelton et al., 2007; Moore and Renfrew, 2005). The design of the SeaWinds instrument, as well as its large swath width, make it ideal for the temporal sampling of rapidly developing mesoscale weather systems (Chelton et al., 2006). To detect small-scale and recurrent spatial patterns induced by the islands of New Caledonia, we use the high spatial resolution and twice-daily QuikSCAT swath product at 12.5 km (hereafter QHR12) available from the Jet Propulsion Laboratory (JPL) at <http://podaac.jpl.nasa.gov/PRODUCTS/p286.html>. Elements about the operations leading to the spatial resolution enhancement of QHR12 and its accuracy are given in Appendix A (and for more details see Hoffman and Leidner, 2005). Our QHR12 regional product based on a dataset of 6244 QuikSCAT twice-daily tracks, presents 10-m equivalent neutral-stability wind mapped on a regular grid ( $0.125^\circ \times 0.125^\circ$ ) for the period of 19-July-1999 to 12-June-2008. Gridded products are more practical than swath products, but the necessary spatial and temporal interpolations used to obtain these datasets result in smoothing the wind speed and reducing its original variance (Mostovoy et al., 2005). Smoothing is amplified in regions where substantial diurnal wind variability occurs and the winds are distorted at a frequency that matches the dominant sampling interval (3–4 days). Using a compositing technique applied on the swath products (explained in Section 2.5), a classification of swaths is conducted to infer the dominant surface circulation regime. This swath by swath classification allows us to represent the daily mean climatology associated with each circulation regime. In addition, the diurnal signal of the winds may be partly retrieved by compositing QHR12 swaths for the two daily QuikSCAT orbital passes over the region (Section 4).

### 2.3. Assessment of effective resolution from wavenumber spectral analysis

The effective resolution of NCEP FNL data, WRF (4-km grid mesh) regional solutions, and satellite observations can be quantified from their wavenumber spectral analysis (Chèry et al., 2004; Milliff et al., 2004; Skamarock, 2004; Chelton et al., 2006). Following the method from Skamarock (2004), we compare the spatial

wavenumber spectra of 10-m wind speed from NCEP FNL and WRF (Fig. 3). The wavenumber spectra of QHR12 wind speed (processing details in Appendix A) is computed over the period 1999–2008 and given in Fig. 3. Also added in Fig. 3 is the slope of the  $k^{-5/3}$  Kolmogorov scaling law, which corresponds to the mesoscale range with wavelengths 10–1000 km. The mesoscale spectral range is not well understood and has explanations involving theories of either three-dimensional turbulence, stratified 2D turbulence, or internal gravity waves dynamics (Skamarock, 2004; Milliff et al., 2004). Nevertheless, the spectral slope  $k^{-5/3}$  is observed in flows with high Reynolds number and is predicted in modeling studies using mesoscale models.

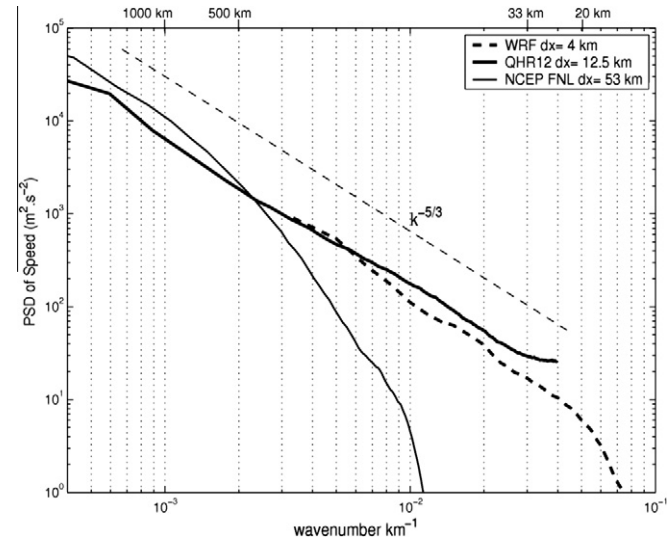


**Fig. 3.** Wavenumber spectra of wind speed over the region computed from WRF (dashed line), QuikSCAT observations from Level 2B 12.5 km (thick line) and NCEP FNL (thin solid line). For comparison, the theoretical slope  $k^{-5/3}$  is represented (thin dashed line).

From Fig. 3, all products show a  $k^{-5/3}$  power-law consistent with theory for the mesoscale spectral range. However, at wavelengths shorter than 1000 km, NCEP FNL displays a sharp drop off, which is also reported and explained by Chelton et al. (2006). These authors show that NCEP FNL underestimates the intensity of synoptic and mesoscale wind variability, despite its grid resolution of about 50 km. In comparison, in the high-resolution grid of the regional model employed in this study, the loss of wind energy only appears for wavelengths shorter than 20 km ( $5\Delta x$ ); the preservation of mesoscale dynamics can be explained by the quality of numerical methods and filters used in WRF (Skamarock, 2004). The spectrum slope of QHR12 follows the theoretical power-law but a buildup of energy is evident in the spectrum tail from wavelengths shorter than 30 km. This buildup of energy in the shorter waves may result from instrumental noise. Our analysis shows that the mesoscale model can improve the existing spatial resolution of atmospheric phenomena in the New Caledonia region, ranging from synoptic-scale events to features as fine as 20 km. The effective resolution of QHR12 (30 km) is comparable with the numerical model, but the satellite product lacks the model vertical dimension, fine temporal resolution and coverage of the land and near-shore areas.

#### 2.4. Model and QuikSCAT validations against station data

##### 2.4.1. Model validation

The *in situ* data used for comparison with WRF are obtained from nine Météo-France weather stations reported in Fig. 1. The hourly data recorded are 10-min means, 2-m surface air temperature ( $T_2$ ) and 10-m wind speed and direction (except at Thio, Moué and Nouméa, where the measurement height is 15 m). The accuracy is  $1 \text{ m s}^{-1}$  and  $10^\circ$  for wind speed and direction, and  $0.1^\circ \text{C}$  for temperature. All stations are located along the shore, except Amedée Light House which is offshore; the time range encompasses the three November–April warm seasons of years 2005–2008. The simulated atmospheric variables are extracted at the closest grid points to each station, and 6-hourly averages are computed for wind vector and temperature of both model and observa-

**Table 1**  
Statistical comparison between model and observations.

	AMEDEE	MAGENTA	NOUMEA	MOUE	TOUHO	THIO	OUANAHAM	NEPOUI	NESSADIOU	ALL
<i>Speed stations (m/s)</i>										
Number of data	2130	1683	1690	1677	1453	1688	1638	1621	1617	15,197
Mean	7.1	4.0	5.8	5.0	4.6	6.5	4.2	3.6	3.9	5.2
Std. dev.	2.7	1.8	2.2	1.8	1.9	3.1	1.9	1.9	1.6	2.5
<i>Model – stations difference</i>										
Bias	-0.5	1.5	0.1	0.6	2.0	0.2	1.9	1.5	0.5	0.8
RMSE	1.7	2.1	1.4	1.2	2.3	2.0	2.2	2.3	1.4	1.9
IOA	0.9	0.8	0.9	0.9	0.7	0.9	0.8	0.7	0.8	0.8
<i>Direction stations (<math>^\circ \text{N}</math>)</i>										
Number of data	1729	799	1236	1158	922	994	833	429	456	8556
Mean	118.3	109.7	101.8	114.4	118.1	110.4	99.5	139.1	156.2	114.9
Std. dev.	36.6	30.4	38.8	49.4	27.7	48.9	31.7	28.5	58.3	41.9
<i>Model – stations difference</i>										
Bias	6.0	13.7	21.7	7.8	11.5	19.3	21.0	6.3	-22.3	11.4
RMSE	19.9	18.6	27.9	35.3	23.7	36.0	36.2	23.7	76.6	32.8
IOA	0.9	0.9	0.9	0.8	0.8	0.8	0.6	0.8	0.4	0.8
<i>T 2m stations (Celsius)</i>										
Nb data	2130	1683	1690	1677	1453	1688	1638	1621	1617	15,197
Mean	25.5	25.1	25.0	24.0	25.7	25.1	25.3	24.8	24.9	25.1
Std. dev.	1.5	1.8	1.9	1.9	1.5	1.3	2.0	2.0	2.3	1.8
<i>Model – stations difference</i>										
Bias	-0.8	-0.5	-0.3	0.7	-0.6	-1.1	0.3	0.4	-0.3	-0.3
RMSE	1.5	1.2	1.1	1.1	1.3	1.3	1.2	1.1	1.2	1.2
IOA	0.8	0.9	0.9	0.9	0.8	0.8	0.9	0.9	0.9	0.9

tions. Observations marked with low wind data (speed < 3 m s<sup>-1</sup>) are removed prior to the statistical computation of wind direction. To summarize the time series behavior, Table 1 provides details of the mean and standard deviations of all observations, along with departure between model and observations. In addition, validation of predicted (*P*) data (from the model) against observation (*O*) was done through statistical performance measures, including the root mean square error (RMSE) =  $\sqrt{[(P - O)]^2}$  and Index of agreement (IOA) =  $1 - \frac{(P - O)^2}{(|P - \bar{O}| + |O - \bar{O}|)^2}$ , based on the recommendation of Willmott (1981). The IOA is a measure of model skills in predicting variations about the observed mean; a value above 0.5 is considered to be good, 1 means a perfect match.

The model is generally in very good agreement with the observations (last column of Table 1). T2 deviation is below 0.7 °C everywhere, except for Thio and Amedée Lighthouse where the model underestimates the mean observations. The RMS error associated with these two stations, as well as Touho station, is large and their IOA is low. Amedée station is lying on a small sandy island, not represented in the model and the model grid point close to Thio and Touho fall in the sea, meaning that surface temperatures are probably less comparable for these three stations. From scores of wind parameters (RMSE, IOA), Nessadiou station, along the west coast, is characterized by the largest difference between the model and wind records. Thio, along the east coast, Ouanaham and Moué, the two most interior land lying stations, also present discrepancies between the simulated and recorded wind directions (RMSE > 35°). In general, the model tends to slightly overestimate the wind speed, especially at Magenta and Touho airfields but, overall, the predicted wind speed and direction are very close to the measurements. Statistics of wind parameters show better skill scores (IOA of about 0.9) for stations lying on the windward side of the Mainland, namely Phare Amedée and Nouméa. Our computed scores reveal that large directional errors are associated with stations lying close to valleys (Nessadiou) or mountainous shores (Thio), suggesting that small-scale orographic circulation remain unresolved at the effective model resolution (20 km). Nevertheless, these scores added to comparisons between QHR12 and WRF shown in Sections 4 and 5 give us confidence in the model's ability to capture the main spatial and temporal variability of the regional and local airflow circulation.

#### 2.4.2. QHR12 validation

QHR12 winds, collocated in time and space, are evaluated using the recorded wind data at the Amedée Lighthouse weather station (AMD, Fig. 1). This station is located on the southwestern tip of the Mainland, along the barrier reef, approximately 20 km offshore, and is representative of marine weather conditions. Table 2 presents comparable statistics using different wind ranges like Sharma and D'Sa (2008) and Tang et al. (2004). The quality of the QHR12 dataset based on this comparison is consistent with the instrument specification of 2 m/s and 20° (Tang et al., 2004) and the accuracy of wind direction is enhanced for high wind speeds.

**Table 2**  
Statistical comparison of QHR12 against wind measurements at Amedée Light House. *R* is the correlation coefficient.

Speed (m/s)		Nb data	Bias	RMSE	<i>R</i>
Station wind speed	≥ 0 m/s	4011	0.3	1.0	0.7
	≥ 3 m/s	3913	0.3	1.0	0.7
	≥ 6 m/s	2716	0.1	1.0	0.5
Direction (°N)					
	Station wind speed				
	≥ 0 m/s	4011	5.9	22.2	0.5
	≥ 3 m/s	3913	4.8	20.6	0.6
≥ 6 m/s	2716	6.0	13.2	0.8	

Note that the weather station is located on the edge of the QHR12 land mask, where measurements may still be land contaminated (Tang et al., 2004). Therefore, QHR12 is not expected to reveal its best assets at this location.

#### 2.5. Classification of regional weather types by clustering

Principal component analysis (PCA) and clustering techniques are widely used to conduct synoptic classification of the climatological regimes identified in observations and model results. Conil and Hall (2006) used PCA combined with two clustering algorithms (a *k*-means and a mixture model clustering method) to establish the regional circulation inferred from simulated high-resolution wind fields over Southern California. In our region, Leroy (2006) applied PCA and a *k*-means clustering method on a dataset of daily sea level pressure (SLP) from ERA40 over the warm months November–April from 1957 to 2002, and isolated four weather regimes. Alternatively, subjective methods are based on an inspection of daily weather maps to identify the most important circulations. Such a method was applied by Lefort (2005) over New Caledonia, identifying seven synoptic weather types. However, cluster analysis is a more objective and reliable approach in the sense that this partitioning method can determine a set of recurring and persistent weather states with no assumptions regarding how the states manifest themselves in the data. The main aspects of our clustering method are presented in this section but more details are provided in Appendix B.

To perform the regional surface circulation classification, the dataset QHR12 of daily satellite surface wind measurements for the Austral summer is projected onto its two leading modes of variability. Fig. 4 shows the result of the PCA conducted on the normalized remote sensed winds to derive the dominant patterns of variability. Using North's criteria (North et al., 1982), the first two leading modes are distinct and explain 40% of the total variance. The values of these two principal components are then clustered into homogenous groups, applying the Gaussian Mixture Model (GMM), as detailed by Smyth et al. (1999). To determine the optimal number of components (cluster) that provide the best fit to the data, we use the criterion from Smyth et al. (1999), based on the cross-validated log-likelihood. An optimal number of four clusters are found to describe the dominant stationary flow regimes represented in the dataset for the nine warm periods of November–April along the years 1999–2008. This number is

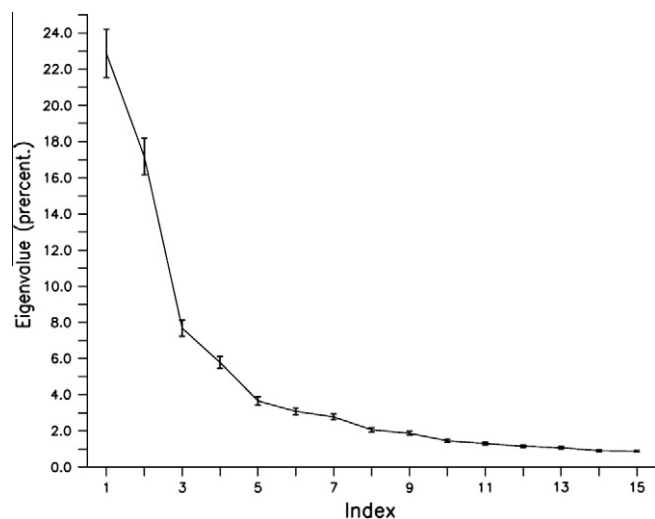


**Fig. 4.** Eigenvalue spectrum, with confidence limits derived from North et al. (1982).

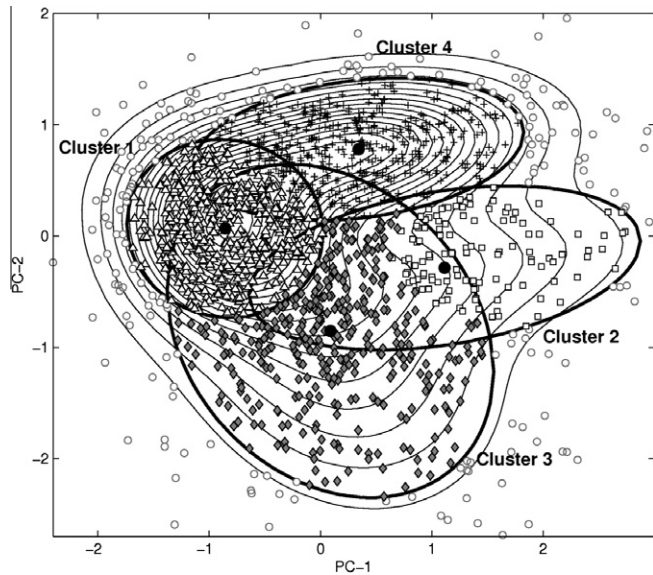


**Fig. 5.** Probability Density Function (PDF) of the QuikSCAT surface wind anomalies estimated by the Gaussian Mixture Model (thin contours). Data anomalies (empty dots) are projected onto the plane spanned by PC-1 and PC-2 for nine warm seasons. Estimated centroids of the four clusters are indicated by the full dots. The extension of the clusters, defining the local circulation regime, is indicated by the ellipses (thick contours), with semi-axes equal to 1.5 standard deviation in each principal direction. Cluster's members are defined with symbols: Cluster 1 (filled triangle), Cluster 2 (empty square), Cluster 3 (filled diamond), Cluster 4 (black crossing), unclassified (empty circle).

consistent with the four weather regimes objectively defined by Leroy (2006) with her  $k$ -means method applied on SLP for the same seasonal period with ERA40 dataset. Fig. 5 shows the contour map of the PDF resulting from the linear combination of the four Gaussian density functions. The extension of clusters 2 and 3, shown by their respective covariance ellipse, is larger than for clusters 1 and 4, suggesting that the spatial variability of the surface circulation associated with regimes 2 and 3 is probably strong, while regimes 1 and 4 are characterized with more steady circulation conditions (see details in Appendix B). The clustering allows us to classify 83% of the nine Austral summer seasons. The local surface circulation patterns related to each weather regime is then constructed by time-averaging the flow over the corresponding days; this is done for the twice-daily QHR12 along track and the hourly WRF outputs. However, only summer days from 2005 to 2008 are used in the construction of the model composite. In addition, all direct comparisons between model and satellite winds in the following are based on a sub-sample of the model solution, where the model data is collocated within 30 min of the QuikSCAT sampling time.

In order to discuss the persistence and transition between each weather type, durations distribution and transition probabilities are investigated following Kondrashov et al. (2007). Then, the Markovian method of Vautard et al. (1990) is applied to assess the most significant transitions between the four weather types. Finally, to identify the connection between local weather regimes and large-scale atmospheric circulation, we derived synoptic composites for the surface and the free atmosphere (adequately captured by the 500-hPa level) from the 1999–2008 NCEP Reanalysis 2 (NCEP2; [http://nomad1.ncep.noaa.gov/ncep\\_data](http://nomad1.ncep.noaa.gov/ncep_data)) by averaging over the days assigned to each regime by the clustering analysis. These composites were constructed for daily SLP, 10-m and 500-hPa winds, as well as 500-hPa omega (pressure vertical velocity), for the same period as the QHR12 dataset. 500 hPa wind fields are also used to follow the equatorial easterlies and the subtropical westerlies, which indicate the strength of the subtropical jet stream core located between 200 and 100 hPa.

### 3. Regional weather types

#### 3.1. Regional composites

Maps of each composite of satellite surface winds are presented in Fig. 6, along with corresponding maps of the model, for the time period 2005–2008. Synoptic maps from NCEP2 are shown in Fig. 7. In general, composites of measured and modeled winds are in good agreement, i.e., the airflow shows similar structure and magnitude. All weather regimes, except Regime 2, exhibit a surface circulation dominated by southeast trade winds.

Regime 1 captures a strong, near steady trade-wind flow over the domain, reaching  $8 \text{ m s}^{-1}$  and is referred to here as ‘Strong SE Trade-wind’. The regional circulation in Regime 4, called here ‘Sub-tropical’ also shows a near steady SE direction, but with weaker winds (stronger in the north), representing the early summer low latitude position of the subtropical high belt (Fig. 7). On the contrary, the circulation in Regime 3 follows the late summer southward shift of the subtropical high belt and SPCZ (Fig. 7). This regime is called ‘Tropical’ and produces winds above  $6 \text{ m s}^{-1}$  in south-western New Caledonia. Regime 2 exhibits a weak easterly airflow circulation. Its spatial variability, as revealed by wind direction, is the largest of the four regimes. We call this regime ‘Weak Easterly Circulation’.

Statistical parameters of satellite and model surface wind composites are computed in Table 4 for the time period 2005–2008. For all regimes, the statistics between observations and model agree very well. The steady Regime 1 is characterized with little variability of wind speed and direction. With only 57 along tracks, Regime 2 is characterized with large variability of its wind direction. A Student’s  $t$ -test was applied to the remote sensed wind and shows that the wind pattern of Regime 2 is not statistically significant at the 95% confidence level (the total number of episodes within each cluster is considered as a conservative estimate of the number of effective degrees of freedom), even though this pattern is confirmed by the model composite. Note that areas of low wind speed in Regimes 2, 3 and 4 coincide with areas of low significance (indicated with diagonal hatching in Fig. 6). Among the four regimes, Regime 1 which is the most robust and steady also shows the clearest island-scale wind structures (of  $\sim 150 \text{ km}$ ). Later in Section 4, we will focus on this regime to further explore the temporal variability and physical processes involved in these island-scale circulations.

#### 3.2. Associated synoptic-scale circulation and seasonal modulation

The NCEP2 dataset is used to relate the mesoscale to the synoptic circulation. The left panels of Fig. 7 show the four low-level airflow regimes and corresponding synoptic circulation. Interestingly, the island-scale structures displayed in the satellite winds of Regime 1 are missing in the NCEP2 composite; this emphasizes the inability of global atmospheric models to resolve those scales (Chelton et al., 2006). The right panels of Fig. 7 show 500-hPa winds and Omega vertical velocity. Negative values of omega represent ascent of warm, moist air, and can be considered as a tracer for the SPCZ (e.g. Vincent, 1994).

The area of strong trade-winds in Regime 1 extends zonally from the North Queensland coast to the south of Fiji, while the convergence zone (associated with strong ascent) is confined over Papua New Guinea and the Solomon archipelago. Regime 1 shows only weak seasonal modulation throughout the austral summer (see the seasonal distribution of weather types in Fig. 8). It coincides with a large and intense anticyclone located over the northern Tasman Sea, associated with a strong air subsidence centered over northern New-Zealand. In late winter and at the beginning

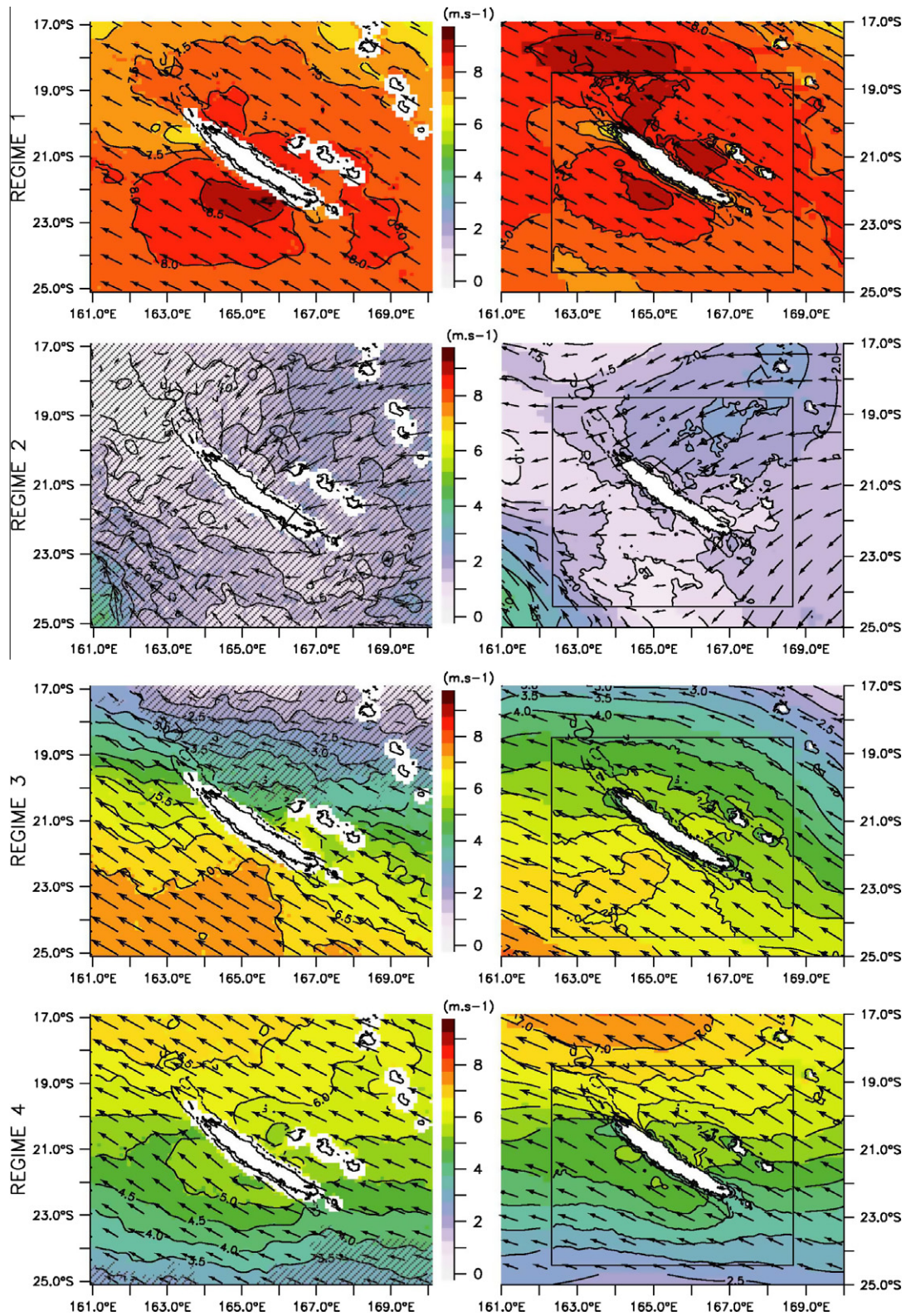


**Fig. 6.** 10-m Neutral equivalent wind composite maps showing the four summer weather types for the period 2005–2008. Left column: satellite observation product QHR12. Right column: WRF model; the boundaries of the innermost model grid are super-imposed. Diagonal hatching indicates regions where the data are not significant at the 95% level.

of the warm season (November–December), the subtropical high system has reached its lowest latitude and result in the predominance of Regime 4 (Fig. 8), which is associated with dryer weather over New Caledonia and strong 500-hPa subtropical westerlies

south of the island. Table 5 shows that the transition probabilities between Regimes 1 and 4 are significant and the related forward and reverse circuits are frequent, occurring in 31% of all observed transitions. At the end of the year, the New Caledonia region comes

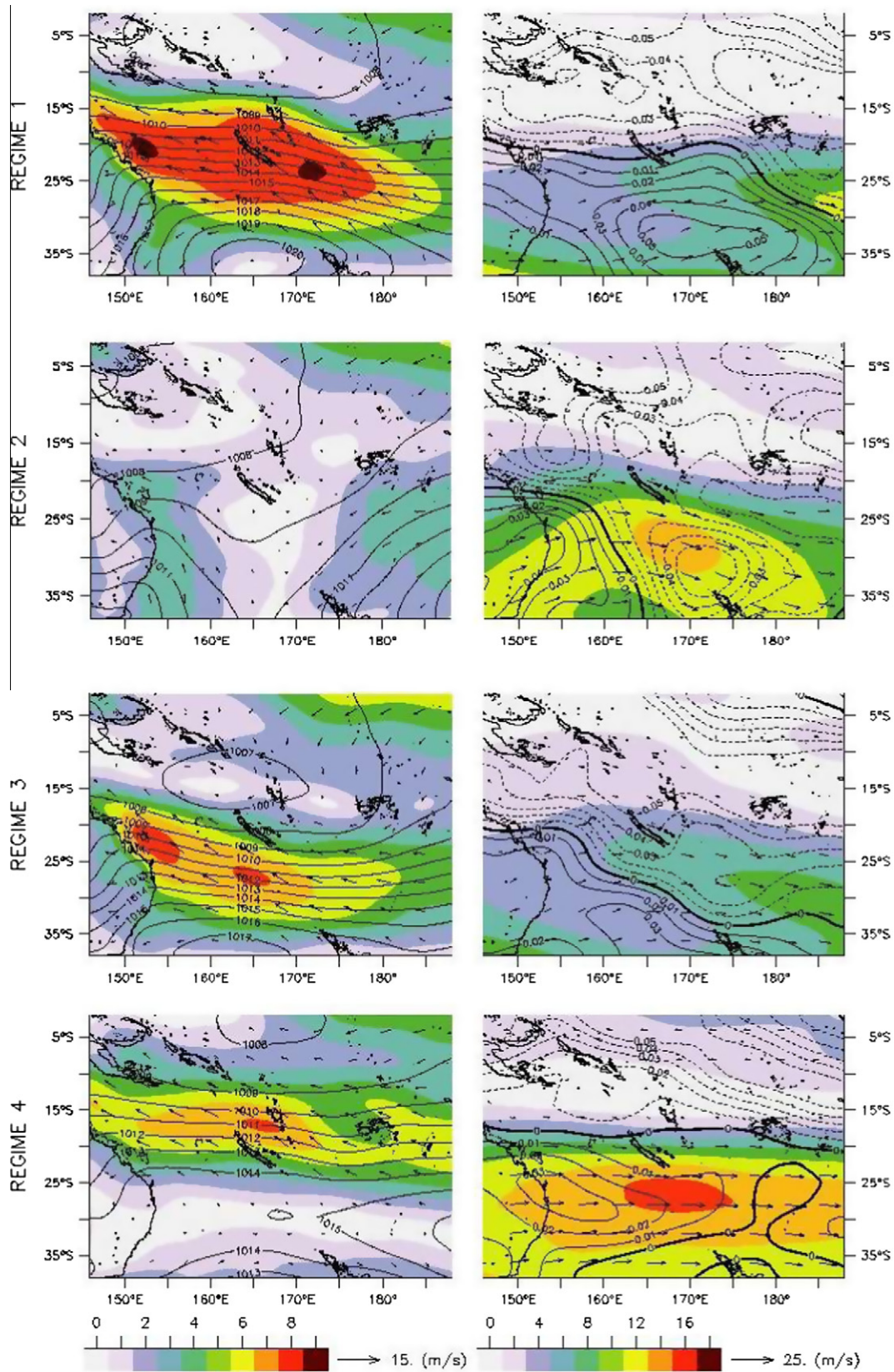


Fig. 7. NCEP2 synoptic maps for the four summer weather types during the period 1999–2008. Left column: 10-m wind speed (colors; units: m/s) and sea surface pressure (contours; interval = 1 hPa). Right column: 500-hPa wind speed (colors, units: m/s) and 500-hPa Omega vertical velocity (contours; interval = 0.01 Pa/s; dashed/negative contours represent ascent).

under the influence of the SPCZ, displaced poleward (Robertson et al., 2006), and the westerlies aloft weaken (Sinclair, 1996). Moisture-laden easterly airflow events associated with Regimes 3 are

more frequent and contribute to producing large amounts of rainfall along the eastern flanks of the Mainland, with increasing precipitation toward the northeastern coast (Météo-France report,

**Table 3**

Statistics of wind composite parameters (speed and direction) computed from the twice-daily QuikSCAT along track observations for the period 1999–2008. Brackets refer to the equivalent percentages.

	Number of		Wind speed (m s <sup>-1</sup> )		Wind direction (°N.)	
	days	orbital pass	Mean	Std. dev.	Mean	Std. dev.
Regime 1	491 (30%)	941 (30%)	8.0	2.2	122.5	21.6
Regime 2	121 (7.4%)	231 (7.4%)	1.4	2.3	120.6	94.8
Regime 3	368 (22.6%)	706 (22.6%)	5.2	2.8	122.9	60.5
Regime 4	443 (27.2%)	854 (27.3%)	5.2	2.2	118.9	45.6
Unclassified	209 (12.8%)	398 (12.7%)	–	–	–	–

2007). Therefore, from January to March, the regional climate is driven by the SPCZ and, accordingly, weather conditions of type 3 are 2–3 times more frequent than at the beginning of the warm season. The Markovian method reveals that circuits 1–3 are significant during this period and occur in 26% of all transitions, suggesting that the meridional shift of the two large-scale features, the subtropical high belt and the SPCZ, triggers these preferred paths (Sinclair, 1996).

In Regime 2, the surface airflow is weak across the whole southwest Pacific domain and subtropical descent is confined to Australia. The pressure high along the west coast of Australia drives cool air from the Tasman Sea to the Coral Sea while the airflow impinging on Fiji is driven by a high pressure system located over the south central Pacific. This regime is associated with a widespread ascent dominating the whole basin and easterly trade-winds may bring warm, moist air to New Caledonia, with favorable rainfall conditions. The Regime 2 rarely persists for more than 6 days (Fig. 9) and is a transient weather type compared with the three other regimes. Transitions 3–2 are significant (Table 5), with an occurrence value equal to 21%.

Each of the four regimes seems to be related to a specific synoptic environment which results from the seasonal position and intensity of the SPCZ, subtropical jet stream, and mid-latitude systems. In the following sub-section, we will show how these connections can explain the role of intra-seasonal and inter-annual modes of variability in modulating the weather type occurrences.

### 3.3. Modulation by large-scale variability: MJO and ENSO

We investigate the link between regional weather types and dominant modes of large-scale atmospheric variability affecting the Pacific Ocean. Two previous studies have attempted to link regional phenomena in the southwest Pacific either to El Niño–Southern Oscillation (ENSO) or the Madden–Julian Oscillation (MJO). Delcroix and Lenormand (1997) use the Southern Oscillation Index (SOI, <http://www.cpc.ncep.noaa.gov/data/indices/soi>) to identify ENSO signature in oceanic and wind data around New Caledonia. Leroy and Wheeler (2008) validate a statistical tropical

**Table 4**

Statistics of wind composite parameters (speed and direction) computed from the twice-daily QuikSCAT along track observations, and WRF collocated in time and space with QuikSCAT for the period 2005–2008.

	Number of		Wind speed (m s <sup>-1</sup> )				Wind direction (°N.)			
	Days	Orbital pass	Mean		Std. dev.		Mean		Std. dev.	
			QHR12	WRF	QHR12	WRF	QHR12	WRF	QHR12	WRF
Regime 1	164 (30.2%)	310 (30%)	8	8.2	2.1	2.3	120.9	119.6	20.3	18.6
Regime 2	30 (5.5%)	57 (5.5%)	1.6	1.8	2.5	2.5	92.7	78.8	101.7	101.7
Regime 3	133 (24.5%)	242 (23.5%)	5.5	5.5	2.7	3	119.4	117.8	59.8	55.1
Regime 4	150 (27.6%)	293 (28.5%)	5.1	4.9	2.2	2.3	118.2	116.6	45.6	45.2
Unclassified	66 (12.2%)	128 (12.5%)	–	–	–	–	–	–	–	–

cyclone prediction scheme in the southwest Pacific, using the Realtime Multivariate MJO index of Wheeler and Hendon (2004, available from <http://www.bom.gov.au/bmrc/clfor/cfstaff/matw/maproom/RMM/index.htm>).

To verify that these large-scale modes of variability have a clear influence on the occurrence of the circulation regimes, we conduct a Chi-square goodness-of-fit test of the null hypothesis (see Leroy, 2006). For each weather regime, the corresponding days are distributed over the  $k$  phases of the investigated large-scale oscillation to derive the observed data distribution ( $O$ ; number of days of occurrence). The null hypothesis (no relation to the large-scale mode) assumes that the distribution of weather types does not depend on the modes of variability, i.e., the expected distribution ( $E$ ). The Chi-square value is a test of this hypothesis:

$$\chi^2 = \sum_{1:k} (O - E)^2 / E$$

Then, the  $\chi^2$   $p$ -value gives the probability that a random distribution provides a value larger than  $\chi^2$ . The  $\chi^2$  goodness-of-fit does not indicate which phases are significant. This is done by the standardized residual  $R = (O - E)/(E)^{1/2}$ , which determines what phases are major contributors to rejecting the null hypothesis. When  $R$  has a magnitude greater than 2.0, the corresponding phase is considered a major contributor to the significance (Hinkle et al., 2003).

Wheeler and Hendon (2004) divided the MJO state into eight phases (named 1–8) and a weak phase. Their Fig. 8 is a composite of low-level (850 hPa) winds and OLR. It shows positive anomalies of convection moving eastward from the western Indian Ocean (phase 1) to the central Pacific (phase 8), and passing over the New Caledonia area during phases 5 and 6. Given the relatively small number of days in each regime (especially in Regime 2), MJO phases are paired to form four categories. In our analysis, weak MJO days are excluded, implying a Chi-square test with 3 degrees of freedom. Tables 6 and 7 show, for each couple of MJO phases, the observed ( $O$ ) and expected ( $E$ ) number of days of each regime, along the standardized residual ( $R$ ). From the small associated  $\chi^2$   $p$ -value ( $<0.05$ ), the null hypothesis is rejected at the 95% significance level indicating that all circulation regimes have a variability significantly related to MJO. Regimes 1, 3 and 4 are very significant. The ‘strong SE trade-wind’ regime is significantly less frequent during phase 5 + 6 which corresponds to convection anomalies over New Caledonia. For Regime 2, it is the opposite. When convection associated with MJO has moved to the east of New Caledonia, the ‘Tropical’ regime (Regime 3) is most frequent while the ‘Subtropical’ regime is unlikely. These results are consistent with the study of Leroy (2006) who showed a similar relationship between MJO and synoptic composites from ERA40.

Warm (El Niño) and cold (La Niña) ENSO phases were defined by taking the standard deviation anomaly of yearly SOI, computed for the period 1958–2008. In our analysis, neutral ENSO conditions are excluded, implying a Chi-square test with 1 degree of freedom. The Chi-square test results from Tables 6 and 7 imply that all circulation regimes, except Regime 2, are significantly influenced

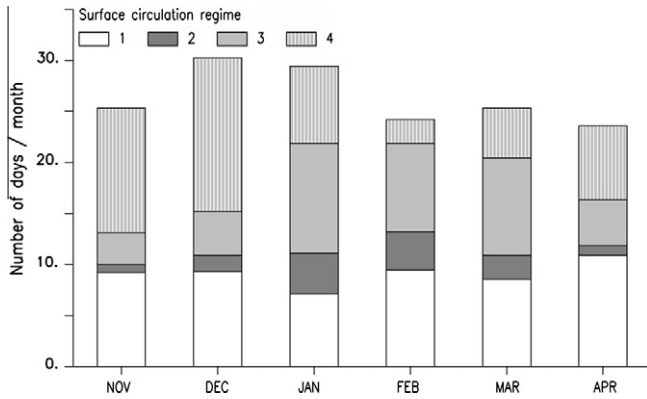


Fig. 8. Monthly mean occurrence of weather types during the warm season.

Table 5

Regime statistics within the austral summer 1999–2008. (a) Transition probabilities between regimes with row and column corresponding to origin and destination, respectively. Transitions that are significantly higher at the 95% level using the Monte Carlo test (Vautard et al., 1990) are in bold letters; (b) number of episodes and mean residence time in each regime.

	Regime 1	Regime 2	Regime 3	Regime 4
<i>(a) Regime transition</i>				
Regime 1	0.12	0.07	<b>0.49</b>	<b>0.54</b>
Regime 2	0.03	0.02	<b>0.26</b>	0.19
Regime 3	<b>0.38</b>	<b>0.67</b>	0.11	0.09
Regime 4	<b>0.48</b>	0.24	0.14	0.18
<i>(b) Size and duration</i>				
Episodes	116	46	93	101
Duration (days)	4.3	2.7	3.9	4.5

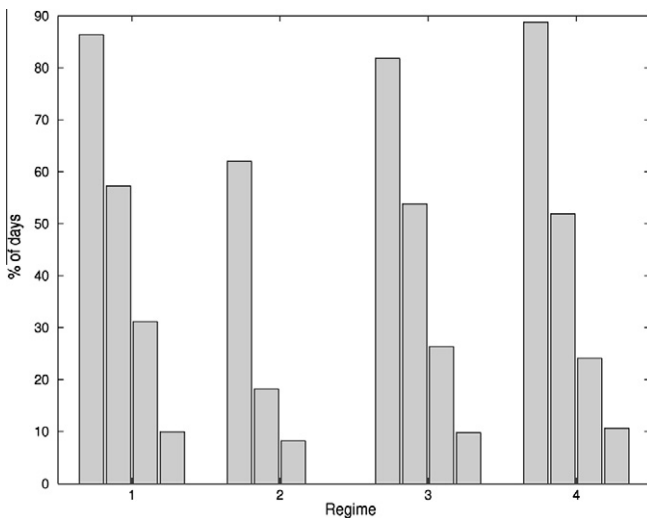


Fig. 9. Percentage of days of each weather type included in homogeneous spells lasting at least 3, 6, 9 and 12 days.

by ENSO. The ‘strong SE trade-wind’ regime is significantly more frequent during warm episodes, while the ‘Subtropical’ regime is negatively affected during cold episodes. The occurrence of the ‘Tropical’ regime is strongly enhanced during cold episodes, the opposite being true during warm episodes. These results are therefore consistent with the findings of Delcroix and Lenormand (1997).

Table 6

Results of the goodness-of-fit test between observed and expected days, assuming that the distribution of the weather type does not depend on MJO phases. *O*: Observed; *E*: Expected; *R*: standardized residual. Absolute values of *R* greater than 2 are in bold; positive (negative) values indicate that regime is likely (unlikely) to occur during the corresponding phase.

		Regime 1	Regime 2	Regime 3	Regime 4
Phases 1 + 2	<i>O</i>	66	12	36	59
	<i>E</i>	58	14	50	51
	<i>R</i>	1.1	−0.7	<b>−2.0</b>	1.1
Phases 3 + 4	<i>O</i>	93	14	49	84
	<i>E</i>	80	20	69	71
	<i>R</i>	1.5	−1.4	<b>−2.4</b>	1.5
Phases 5 + 6	<i>O</i>	55	32	81	81
	<i>E</i>	83	21	72	74
	<i>R</i>	<b>−3.1</b>	<b>2.4</b>	1.1	0.9
Phases 7 + 8	<i>O</i>	76	15	85	34
	<i>E</i>	70	18	60	62
	<i>R</i>	0.7	−0.6	<b>3.2</b>	<b>−3.6</b>
Chi-square	<i>p</i> -Value	0.004	0.035	<0.001	<0.001

Table 7

Same as Table 6, but assuming that the distribution of the weather type does not depend on ENSO phases.

		Regime 1	Regime 2	Regime 3	Regime 4
Warm phase (El Niño)	<i>O</i>	195	32	90	160
	<i>E</i>	168	35	137	138
	<i>R</i>	<b>2.1</b>	−0.5	<b>−4.0</b>	1.9
Cold phase (La Niña)	<i>O</i>	146	39	188	120
	<i>E</i>	173	36	141	142
	<i>R</i>	<b>−2.1</b>	0.5	<b>3.9</b>	−1.9
Chi-square	<i>p</i> -Value	0.003	0.480	< 0.001	0.008

#### 4. Orographic and diurnal circulations around New Caledonia

In the previous section, we have shown that the mesoscale wind pattern related to the strong SE trade-wind regime (Regime 1) is spatially complex, with sharp wind speed variations along the mountainous coast of Mainland New Caledonia. In this section, we will focus on the physical processes involved in the atmospheric spatial and temporal variability induced New Caledonia’s mountain range.

The Mainland is characterized by sharp changes in elevation (Fig. 1) and vegetation type. The eastern coast of the island is wet with a narrow coastal band surrounded by a steep mountain range, while the relief of the west coast is shallower with broad plains and is relatively dry. Modulation of the mesoscale wind circulation in the vicinity of the Mainland is expected from two main sources: land–sea thermal contrasts and orography (Leopold, 1949; Yang and Chen, 2008). Thermal forcing can also be affected by orography, due to differential solar heating of the valley slopes, which may drive gravity currents adding up to land–sea breeze effects. In the following, the model will be used to analyze Regime 1 mesoscale flow around New Caledonia. This analysis relies on the realism of the model solution. Therefore, reliability is first inferred from a finer comparison to satellite measurements, where composite maps are generated for shorter time periods corresponding to twice daily satellite orbital passes over the region. Fig. 10 displays the remote sensed wind composites at 05–07 LST (early morning) and 17–19 LST (late afternoon), along with the simulated wind composites. The comparison shows that the model reproduces properly the strong diurnal variations as well as mesoscale spatial structures resulting from the interaction of trade winds with the islands. Some features appear over-emphasized in the model (see

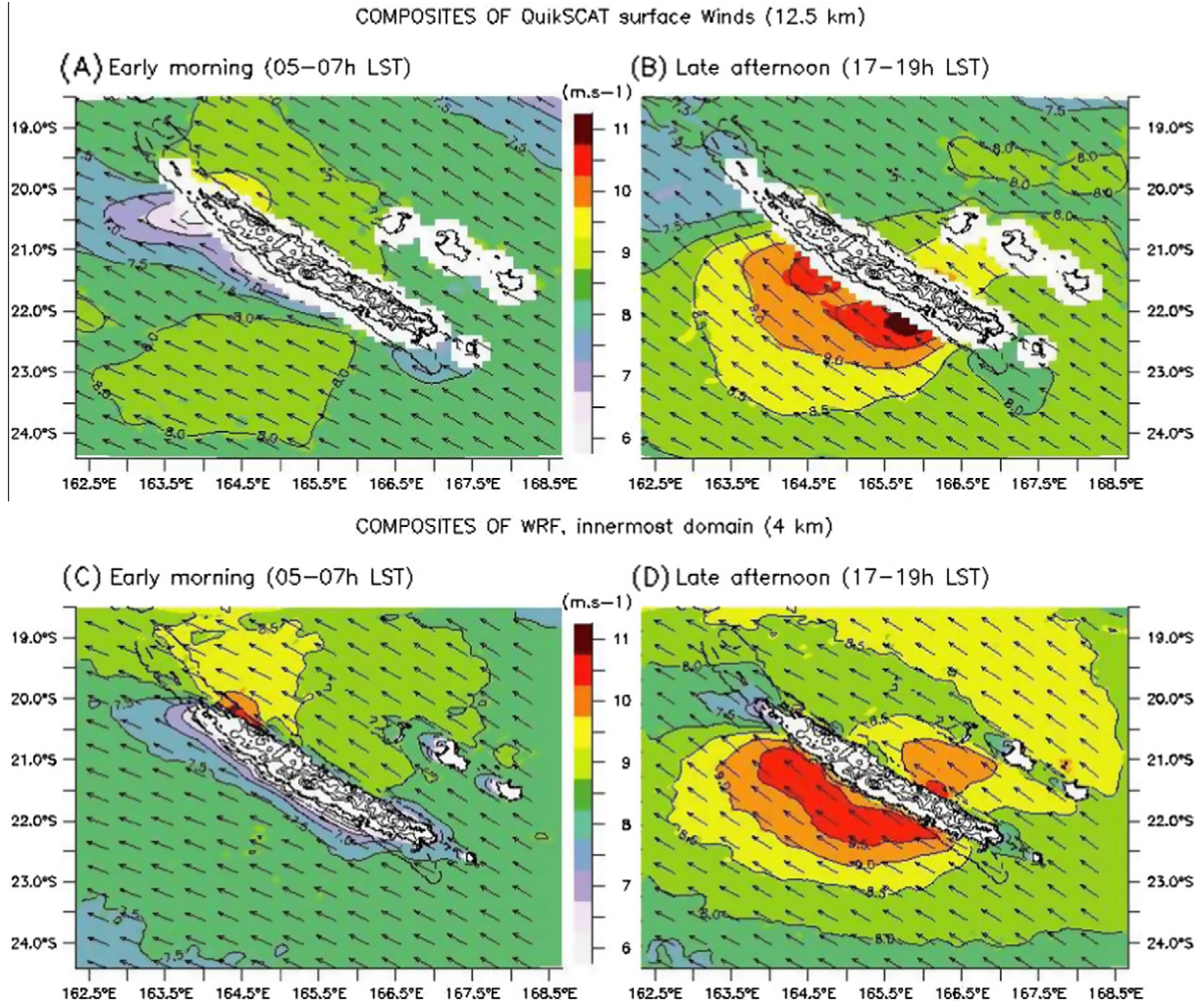


**Fig. 10.** Observed and simulated 10-m neutral equivalent wind composite maps for early morning (05–07 LST) and late afternoon (17–19 LST) of Regime 1 (strong SE trade-wind). The time ranges correspond to the two daily QuikSCAT orbital passes over the region.

section below on nocturnal drainage flow) while others may be undermined (upstream blocking effects), but all spatial and temporal features are present in the model, consistently with observations. They will now be separately analyzed in more details.

#### 4.1. Orographic circulation

We use known results from analytical and idealized 2D and 3D models to investigate the general character of trade-wind flow past the mountain ridge of New Caledonia. The terminology used here to describe orographic effects is illustrated in Fig. 11.

##### 4.1.1. Scaling parameters

The behavior of a stratified airflow past an isolated mountain is characterized by two free parameters, the local Froude number  $Fr_m$ , defined by  $(U/Nh_m)$  and the Rossby number  $Ro$ , defined by  $(U/fL_m)$  where  $U$  is the wind speed,  $h_m$  is the height of the mountain range,  $f$  is the Coriolis parameter,  $L_m$  is the half width of the barrier,  $N$  is the buoyancy frequency (Pierrehumbert and Wyman, 1985). These parameters, scaled with mountain dimensions, express the balance of geophysical forces, i.e., the relative importance of inertial and gravitational forces ( $Fr_m$ ), and of inertial and Coriolis forces ( $Ro$ ). Smith (1989) introduces two other free parameters, the non-dimensional mountain height ( $\hat{h} = Nh_m/U = 1/Fr_m$ ) and  $\beta$  its aspect ratio defined as the ratio between its half-width ( $L_m$ ) and its half-

length ( $l_m$ ). Another useful parameter for our scale analysis is the Burger number ( $B = h_m N / f L_m = Ro / Fr_m$ ), expressing the effect of stratification or the hydrodynamic steepness of the mountain range (Overland and Bond, 1995).  $\hat{h}$  can be regarded also as expressing hydrodynamic steepness, but with respect to inertial rather than Coriolis forces (Ólafsson and Bougeault, 1997).

The cross-stream section AB (Fig. 1b) is used to build the upstream vertical sounding shown in Fig. 2, and to compute the scaling parameters. The trade-wind air-stream impinging on New Caledonia is characterized by neutral and near vertically uniform thermal stability. Between 2300 and 3000 m, the marine atmospheric boundary layer (MABL) is bounded with a strong inversion layer (the trade-wind inversion). The mean flow and background thermal static stability are calculated from the upstream velocity and temperature structure, following the bulk method from Reinecke and Durran (2008). The stably stratified upstream layer is defined between the ground, with  $\Theta_0 = 296$  K, and the lower limit of the strong inversion layer  $h_0$ . From this layer, which is roughly twice the mountain height, we estimated  $\Delta\Theta = 8^\circ\text{C}$  and  $h_0 = 2250$  m. In the bulk method, the total change of  $\Theta$  between the ground and  $h_0$  is used to characterize stability,  $N^2 = (g/\Theta_0 \times \Delta\Theta/h_0)$ .  $U$  is obtained by integrating from the surface to  $h_0$ . The parameters are summarized in Table 8. The Mainland is approximated as an elongated mountain oriented along stream with a mean altitude of 800 m, as represented in the model after

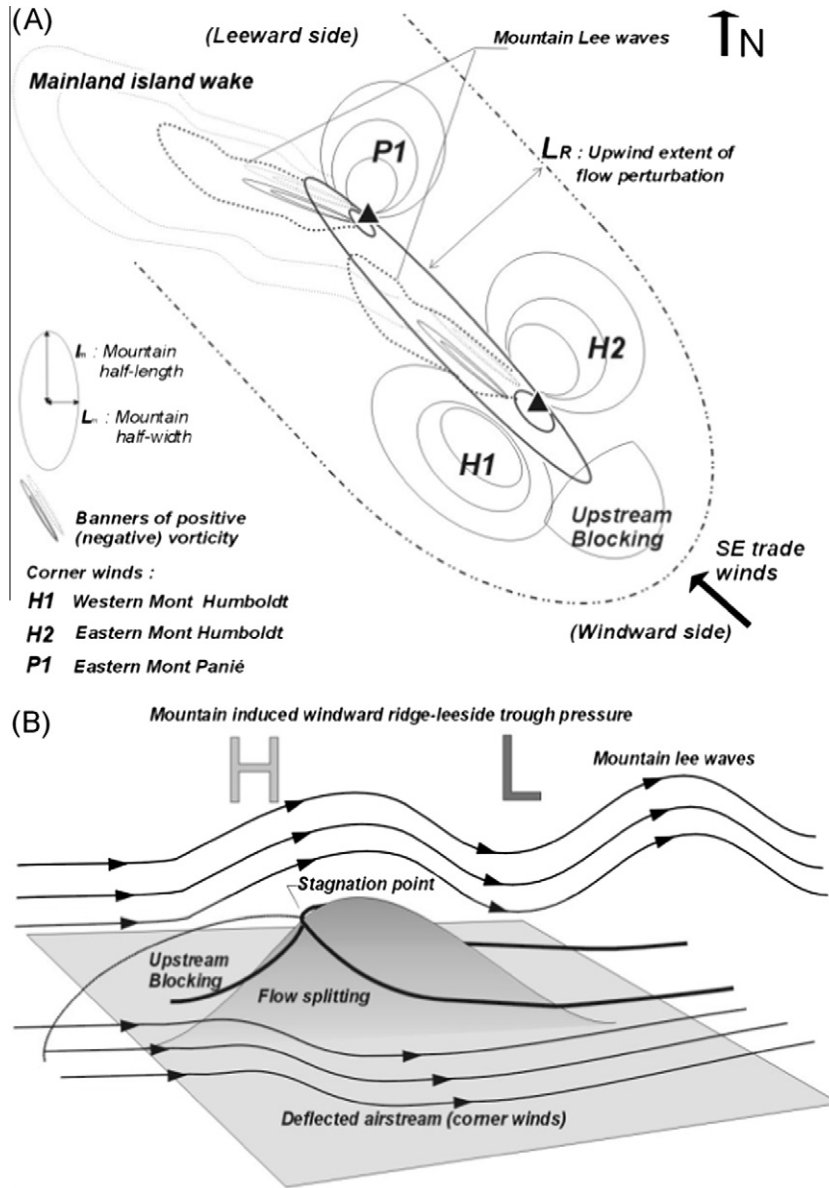


**Fig. 11.** (a) Schematic sketch illustrating the mesoscale structures associated with the perturbed airflow; some elements of the terminology employed in this text are displayed. (b) Example of trade-wind obstruction by a mountainous island and induced flow features, adapted from Smith (1989).

**Table 8**  
Geophysical scale parameters.

Variable definition	Mainland	Mout Panié	Mout Humboldt
$h_m$ (m) Mountain height	800	1600	1600
$L_m$ (km) Mountain half-width	25	5.5	11
$l_m$ (km) Mountain half-length	200	17	25
$f$ ( $s^{-1}$ ) Coriolis parameter	$-5.6 \times 10^{-5}$	$-5.6 \times 10^{-5}$	$-5.6 \times 10^{-5}$
$N$ ( $s^{-1}$ ) Thermal static stability	$10^{-2}$	$10^{-2}$	$10^{-2}$
$U$ ( $m s^{-1}$ ) Incident flow	8.3	8.3	8.3
$Fr_m$ Local Froude number	1.0	0.5	0.5
$B$ Burger number	6.0	52	26
$Ro$ Mountain Rossby number	6.0	26	13
$L_R$ (km) Rossby deformation radius	150	150	150
$\hat{h}$ Non-dimensional mountain height	1.0	1.9	1.9
$\beta$ Mountain aspect ratio	0.13	0.32	0.45

orography smoothing. Scale analysis applied to the Panié and Humboldt ridges is also investigated, but with true dimensions, to take into account these two main orographic singularities.

#### 4.1.2. Island blocking and flow splitting

A parameter widely used to predict topographic flow blocking is the non-dimensional mountain height. When  $\hat{h}$  is roughly greater than 1, the low-level flow is unable to climb the mountain. Instead, the flow is blocked, i.e., dense air piles up above the upstream slopes and a local high is formed reducing the flow speed (according to the Bernoulli equation). Mountain waves aloft add to this high pressure anomaly (Bauer et al., 2000). However, according to the linear theory investigated by Smith (1989) and applied to elliptical mountains, the high pressure formation is reduced for hills aligned with the flow ( $\beta \ll 1$ ), as a consequence of the more rapid dispersion of wave energy aloft. Bauer et al. (2000) established the blocking dependency to the aspect ratio  $\beta$  (see his Fig. 14b), using an idealized, stably stratified, irrotational and inviscid 3D model. For a flow with  $\hat{h} = 1.9$  (Mont Humboldt and Mont

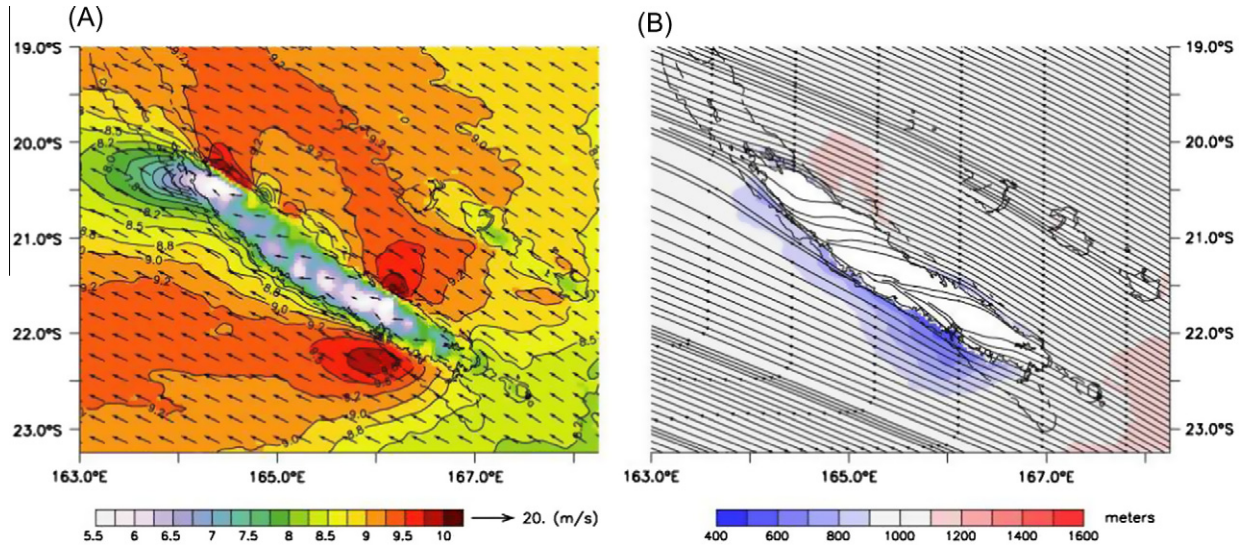


**Fig. 12.** (a) Model daily mean wind speed in Regime 1, vertically-averaged over the planetary boundary layer (filled contours; interval =  $0.25 \text{ m s}^{-1}$ ). (b) MABL height with streamlines overlaid (computed at the first half sigma level).

Panié), the velocity reduction on the windward slope could reach 60% with  $\beta = 0.25$  (Mont Panié) and 150% with  $\beta = 0.5$  (Mont Humboldt), implying flow reversal. In the rotating case, the Coriolis force tends to inhibit blocking by forcing an adjustment to geostrophy (Pierrehumbert and Wyman, 1985; Overland and Bond, 1995). However, with hydrodynamically steep topography, blocking inhibition is minor but the deceleration zone grows upstream to a width defined by the Rossby radius of deformation  $L_R = U/f$  (Overland and Bond, 1995).

This scaling applied to the Mainland yields an estimation of upstream blocking extension of about 150 km. This is consistent with estimations from the observed winds in Fig. 10a and b (spatial scale of about 100 km at sunset and 150 km at sunrise). The upstream blocking represented in the model is narrower, with seaward extension below 50 km (Fig. 10c and d). This result reflects a shortcoming of the model to adequately represent the orographic blocking effect due to topographic smoothing ( $\hat{h}$  is reduced by smoothing in the model).

When the flow is blocked, it is diverted around the edges of the mountain in a process called flow splitting (see Fig. 11b). For  $\hat{h}$  greater than 1, a stagnation point can develop on the windward slope. At a stagnation point, the center streamline splits and passes around the hill on both sides and flow splitting occurs. Fig. 12a and b show, respectively, the model wind vectors averaged over the MABL and surface streamlines. The simulated streamlines clearly show the formation of flow splitting on the upstream slopes of Mont Humboldt and Mont Panié. The flow splitting leads to distinct acceleration at the edges of the mountains (away from the high pressure); these corner winds (or tip jets; Petersen et al., 2005) are denoted H1 and H2 for Mont Humboldt and P1 for Mont Panié in Fig. 11a. Then, mountain lee waves are generated over the ridge. A closer inspection reveals that the lee-wave pattern of Mont Panié extends seaward, while the lee waves of Mont Humboldt affect the ground layer over the Central mountain range. A relative vorticity analysis (not shown) also reveals the formation of banners of negative and positive vorticity downstream of the two main obstacles. These features may generate turbulent processes downstream of the mountain crests (Bauer et al., 2000).

As an averaged obstacle to the trade winds, Mainland New Caledonia is weakly nonlinear with an intermediate value of non-dimensional mountain height  $\hat{h} = 1$ . In this case, a long straight

wake can form downstream of the island mass (Burk et al., 2003; Smith et al., 1997). In Fig. 12b, the streamlines show that a straight wake forms in the northwest quadrant of the island; the two side streams of the wake separate roughly at locations downstream of Mont Humboldt (where a bend in coastline is apparent; see Fig. 1) and Mont Panié. The Mainland island wake appears locally modulated by the smaller-scale circulation associated with the two main obstacles.

Finally, the Coriolis force would only have a relatively minor effect on flow splitting around New Caledonia. High values of Rossby and Burger numbers indicate hydrodynamically steep slopes where the flow is not expected to be geostrophic (i.e., the flow does not remain perpendicular to the pressure gradient). Indeed, no sensitive enhancements of the H2 corner wind by a geostrophically adjusted barrier jet are apparent in the model or observations. However, the offshore influence of the mountain, given by the Rossby radius of deformation  $L_R$  (150 km), is consistent with the modeled (and observed) corner winds H1, H2 and P1. At the island scale and for more zonally orientated winds, i.e., lower island Rossby number, the situation may be different regarding the possible formation of a barrier jet on the northern tip of the Mainland (Petersen et al., 2005).

#### 4.2. Diurnal cycle

To investigate the diurnal heating cycle around New Caledonia, a PCA is conducted on model surface fields following Ludwig et al. (2004). Here, we use the hourly simulated surface winds and 2-m air temperature ( $T_2$ ) spanning the time period 10-February-2006 00:00 UTC to 21-February-2006 00:00 UTC. This time range encompasses a long-lived, persistent Regime 1 episode, so the diurnal cycle that we studied describes a near steady SE trade-wind circulation. The time series is high-pass filtered with a 36-h running mean.

Fig. 13 displays the spatial patterns and time cycle associated with the first leading mode of diurnal variability of surface winds (30% of variance explained) and surface air temperature (80% of variance explained). The diurnal cycle is reconstructed from hourly means of their principal component time series, normalized to place the dimensions of the data in the spatial eigenvectors. Fig. 13a shows a clear land-sea breeze pattern with a convergence (divergence) line aligned with the mountain range during daytime

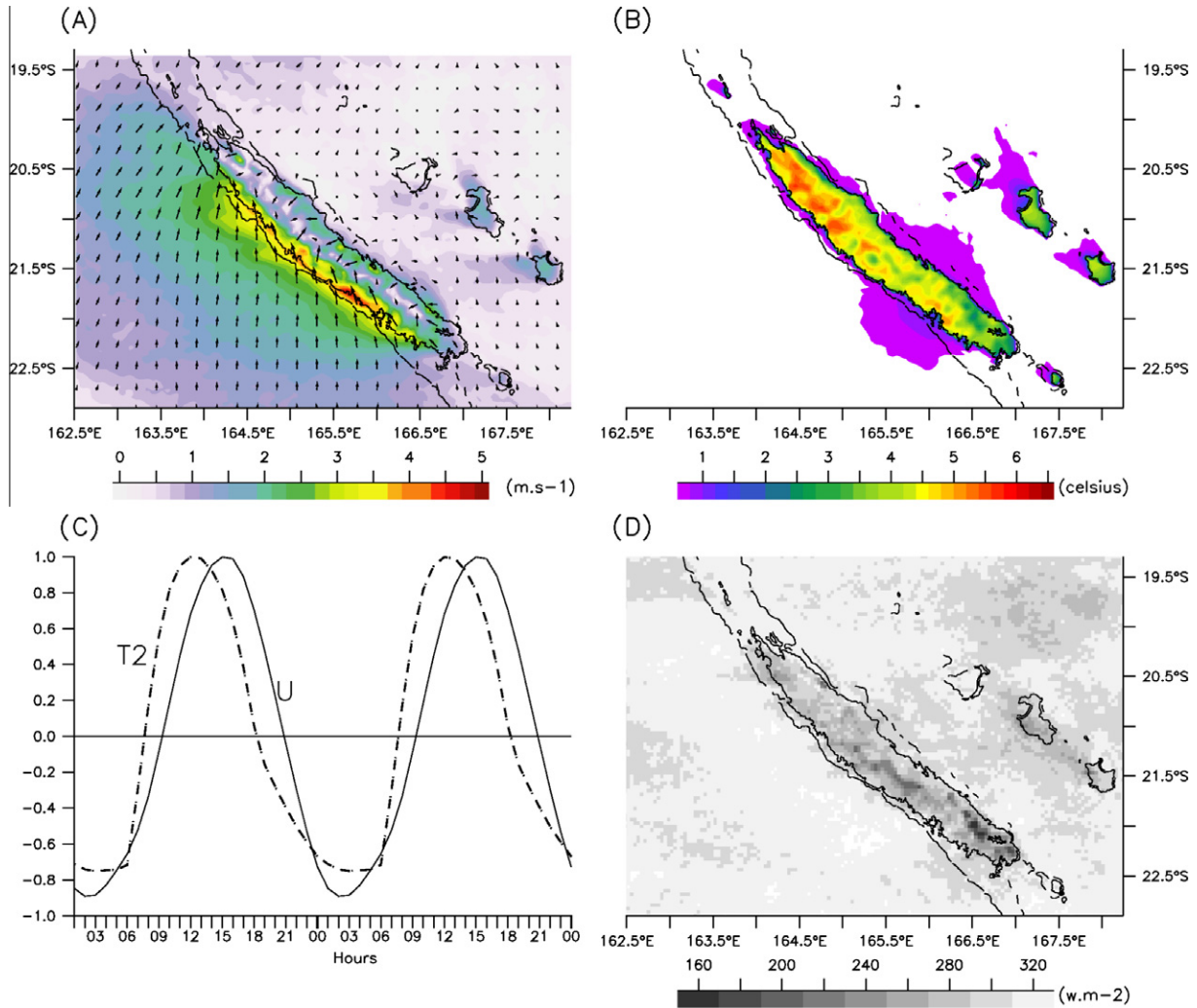


**Fig. 13.** First leading mode of diurnal variability during a long spell of strong SE trade-wind conditions (10-February-2006 00:00 UTC to 21-February-2006 00:00), computed from WRF hourly simulated fields. (a) Spatial pattern and amplitude of diurnal surface wind  $U$ . (b) Spatial pattern and amplitude of 2-m air temperature  $T_2$ . (c) Diurnal cycle of  $T_2$  and  $U$  normalized by the 24-hourly mean of their respective principal component time series. (d) Solar radiation averaged from hourly simulated fields during the same time period.

(nighttime). As shown in Fig. 13c, the diurnal surface wind presents a time-lagged correlation with diurnal  $T_2$ , implying that the wind in Fig. 13a is thermally driven. The diurnal wind maximum (1500 LST) occurs 3 h after the temperature maximum (1200 LST), and reverses in the evening (2100 LST). In the morning, the transition from land to sea breeze (0900 LST) occurs when the land-sea thermal contrast becomes sufficiently strong.

The model diurnal wind pattern and amplitude seems consistent with observations at meteorological land stations. This is revealed by comparing our results with the climatological atlas produced by Météo-France (2007). We also added a more direct comparison of diurnal amplitudes (Table 9) for nine of the stations (those used in Section 2.4). It appears that the diurnal amplitudes are generally in good agreement and that model errors have similarities in pattern with those described in the validation of sub-diurnal frequencies (Table 1, Section 2.4.1).

#### 4.2.1. Land-sea breeze

Along the relatively dry west shore, land-sea breeze is felt far offshore to a distance of 50–100 km (isotach  $1.5 \text{ m s}^{-1}$ ), while the diurnal wind pattern is weaker and confined to a narrower coastal strip band along the east coast, with an offshore extension below 25 km. Wind speed differences between western and eastern

shorelines can reach  $2 \text{ m s}^{-1}$ . On the windward side of the Mainland, land-sea breeze is weaker than along the edges. The diurnal wind is driven by surface temperature contrasts between lowlands and the ocean. It explains why the regions of dry, wide lowlands on the western side experience the largest breeze. Temperature anomalies can also be advected with the trade winds, as happens for example for cold air plumes produced from nocturnal cooling in the leeside of Lifou and Maré Islands. However, orography may contribute to lowering the thermal contrasts. The Mont Panié signature for example is characterized with an absence of thermally driven diurnal winds along its lower slope. Reduction of solar radiation flux (Fig. 13d) as a consequence of orographic cloud cover is probably the main contributor to land-sea breeze inhibition. The main places affected by cloud cover apart from Mont Panié are Mont Humboldt, the Central Mountain Range, and the windward region where stagnation of incoming trade wind cumuli is often encountered (compare diurnal temperatures and solar radiation in Fig. 13b and d).

#### 4.2.2. Nocturnal drainage flow

By a different process, mountain slopes are also a source of momentum in the form of drainage flows which may combine with lowland land breeze effects. Drainage flows are shallow gravity

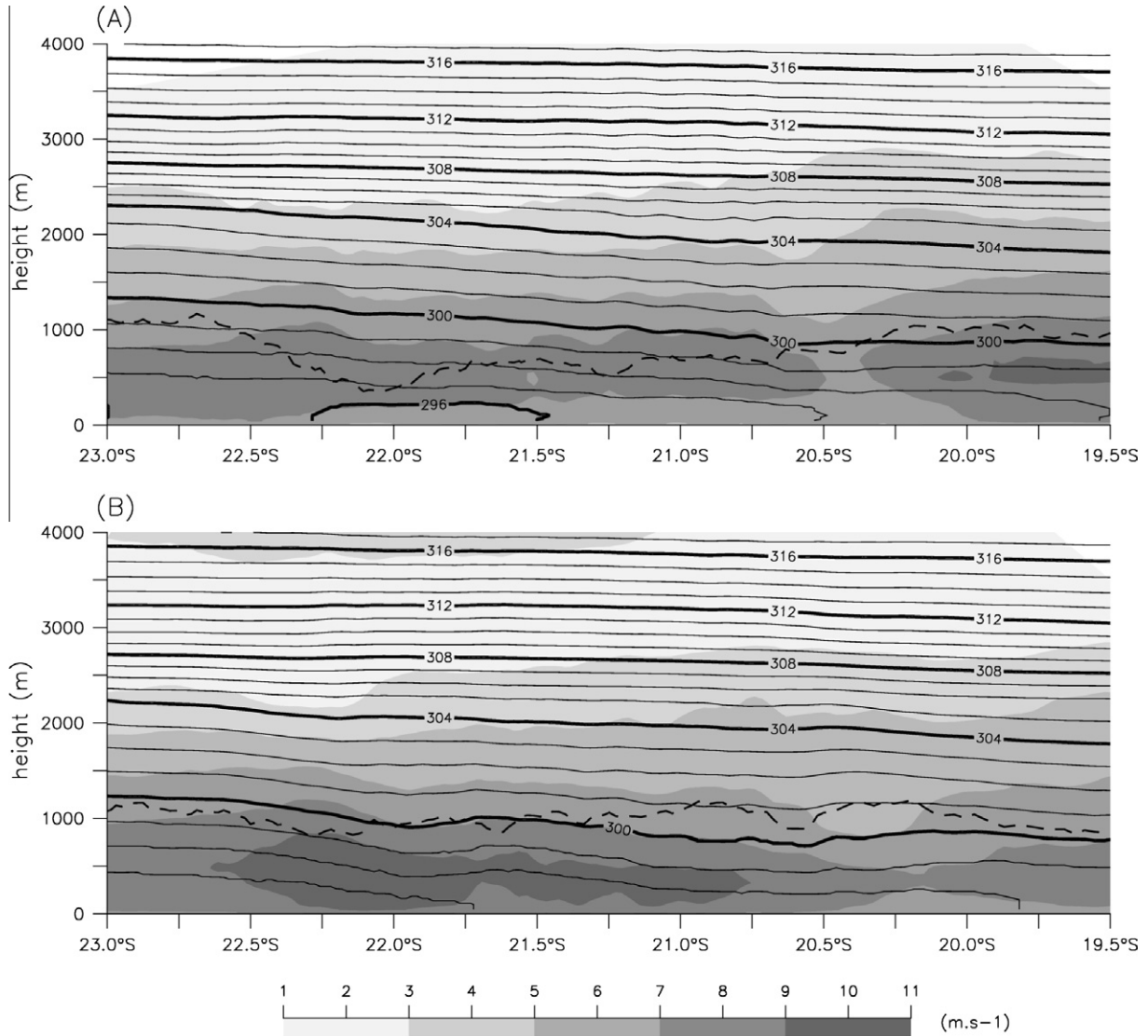


**Fig. 14.** Section CD (Fig. 1) of model atmospheric characteristics along the west coast of Mainland New Caledonia for the Strong SE trade-wind regime: (a) early morning and (b) late afternoon. The variables are: wind speed (shaded; units: m/s), potential temperature (contours; interval = 1 Kelvin) and planetary boundary layer (thick dashed line).

**Table 9**

Diurnal amplitude of surface wind speed and temperature computed from hourly means in the model and observations between 10-February-2006 and 21-February-2006 UTC.

	AMEDEE	MAGENTA	NOUMEA	MOUE	TOUHO	THIO	OUANAHAM	NEPOUI	NESSADIOU
<i>Speed (m/s)</i>									
Model	1.3	4.1	3.1	2.7	1.8	1.6	2.3	5.9	5.0
Observation	1.7	4.1	3.8	3.9	2.4	7.0	3.6	5.7	5.2
<i>T2 m (°C)</i>									
Model	0.8	3.2	2.4	4.8	1.0	1.7	3.8	5.5	5.6
Observation	3.7	3.3	3.7	5.4	3.7	1.6	5.3	5.8	7.5

currents driven by strong cooling on steep, high slopes; their magnitude varies with temperature cooling and mountain steepness. The simulated diurnal  $T_2$  (Fig. 13b) displays a pool of cold air over the shallow waters in the southern part of the west coast, along the western flank of the Humboldt ridge. In this area, the combination of steep slopes and clear skies (Fig. 13d) may cause the formation of cold air drainage flow (Soler et al., 2002). The cold air signal extends well offshore to a distance of 30 km (isotherm 1 °C) and interacts with the warm trade-wind flow, as illustrated in Fig. 10c.

The simulated surface circulation is strongly affected by the nocturnal cooling along the west coast, but this perturbation seems to be less dramatic in the satellite observations. As orographic roughness due to subgrid-scale topography is not represented in WRF, drainage flows from the mountains are probably over-estimated (Jourdain and Gallée, 2010). The difference may also result from the inaccurate representation of roughness due to vegetation. The role of air-sea coupling (missing in the model) is unclear, particularly in the occurrence of summer upwelling events (see Marchesiello et al., 2010).

The weakening of simulated surface winds along the southwest coast is a consequence of nocturnal drainage flow generated on the western slopes of the Humboldt ridge and expanding down-slope towards the ocean. To investigate how the cold pool interacts with the marine layer trade-wind flow, a vertical section (section CD, Fig. 1b) is built from the simulated atmospheric fields of Regime 1 in early morning and late afternoon. At sunrise (Fig. 14a), after nocturnal cooling over land, the cold tongue spreads on the sea surface. This inhibits the vertical turbulent mixing of momentum from aloft to the surface and results in a shallowing of the MABL (see Fig. 12b for an illustration of the MABL shallowing extension) and a deceleration of surface winds. Downwind (around 20.5°S) the airflow enters the Mainland island wake, associated with reduced winds in the leeside and increased winds in the side streams of the wake (downstream of the P1 corner wind). In late afternoon (Fig. 14b), the diurnal circulation has an opposite effect to the trade winds as the sea breeze combines with corner winds to strengthen alongshore winds.

Our results point to a strong modulation of the island-scale circulation by the diurnal heating cycle in the vicinity of the Mainland. With nocturnal cooling, the stabilized environment tends to uncouple the low-level circulation from the trade-wind circulation aloft and some mesoscale orographic features appearing as strong jets during daytime seem to disappear. It is noteworthy that our processing of QHR12 data, by compositing and splitting the swath dataset for each one of the two daily QuikSCAT orbital pass, is valuable to infer the diurnal modulation of the low-level mesoscale circulation around New Caledonia. Our numerical investigations are in agreement with the spatial and temporal variability of satellite measurements. In addition, the model allows us to retrieve the information hidden by the scatterometer land mask. Therefore, it gives us confidence for further investigation, particularly if resolution is increased.

## 5. Summary and conclusion

In this study, a mesoscale model with a 4-km resolution is used in concert with high spatial resolution QuikSCAT surface winds to investigate the spatial and temporal variability of the summer surface circulation around New Caledonia. Our analysis provides the first synthetic analysis of structure and dynamics of the regional and island-scale circulation. In particular, it allows an assessing of thermally and orographically induced flows, which were previously inaccessible from the scattered information collected out of synoptic land weather stations.

Four mesoscale circulation patterns are identified during the November–April season using a cluster analysis method. The ‘strong SE trade-wind’ regime is the most frequent weather type, accounting for slightly less than a third of the austral summer days and is characterized by steady and high southeasterly winds of about  $8 \text{ m s}^{-1}$ . This circulation is associated with a strong anticyclonic feature located in the northern Tasman Sea and is evenly distributed along the season. The other weather types are more seasonal, with transition paths to the first regime, and seem to result from the meridional displacement of the SPCZ, subtropical jet stream, and mid-latitude systems. Occurring for 27% of the days, the ‘Subtropical’ regime is more frequent in early summer (November–December) when the subtropical high and SPCZ are at low latitude. The ‘Tropical’ regime, accounting for 22% of the days, occurs more frequently during the warm and wet period from January to March. Over New Caledonia, these are months with an increased prevalence of weather conditions associated with light wind conditions and high precipitations. Finally, the ‘weak easterly’ regime is the most transient and least robust, accounting for less than 7% of the days and characterized by

very light winds (below  $2 \text{ m s}^{-1}$  over the region) with variable direction.

To determine to what extent the variability in each season is related to the El Niño–Southern Oscillation and the Madden–Julian Oscillation, the frequency of occurrence of the flow regimes was analyzed. On intra-seasonal time-scales, there is a statistically significant modulation of the circulation regimes related to the MJO signal. During the active phase of MJO over the region, there is increased occurrence of the ‘Tropical’ weather type, at the expense of the two dominant weather types. There are also large year-to-year variations in circulation regimes frequency that are related to ENSO. The relationship with ENSO is clearly evident from the occurrence anomalies of the regimes that are associated with meridional displacement of the SPCZ. Positive occurrence anomalies of the ‘strong SE trade-wind’ regime also coincide with El Niño. While our analysis shows a clear relationship between the four dominant weather regimes and the latitudinal excursion and intensity of the tropical and subtropical features (SPCZ, jet stream and the high pressure belt), further investigations should address to what extent these large-scale signals modulate the local climate. For example, it would be useful in terms of predictability to identify how these signals control the break and onset of weather regimes, or to determine if perturbations in the structure of circulation regimes are indicators of the onset of extreme events (Robertson et al., 2006; Leroy and Wheeler, 2008).

The island-scale circulation analysis of the prevalent ‘strong SE trade-wind’ regime reveals the influence of orographic and thermal forcing and confirms anecdotal reports of trends from sailors and the local weather service. The processing applied to the QuikSCAT swath product allows us to overcome the non-uniform spatial–temporal sampling of the scatterometer and to avoid improper estimates in data gaps, such as those introduced in gridded products (Mostovoy et al., 2005). In this case, comparisons between weather observations and the equivalent compositing of the model solution clearly show the ability of the mesoscale model WRF to capture the island-scale circulation and its spatial and temporal variability. This result has convinced us to lead some preliminary investigations of the physical processes involved in the island-scale circulation. Our analysis shows that the mountain range of New Caledonia is hydrodynamically steep and as a result of trade-wind obstruction by the mountainous island, the flow is shaped by coastally trapped mesoscale responses with a spatial scale of about 150 km. Two main obstacles, Mont Panié and Mont Humboldt play a significant role on the dynamical behavior of the low-level flow. Upstream orographic blocking, flow splitting and the formation of mountain lee waves are present both in the satellite sensed and simulated wind pattern and can be explained by the linear theory of stratified flow. The characteristics of wind jets along the Mainland edges (across Mont Humboldt and Mont Panié) are consistent with corner winds evolving from blocking and flow splitting processes, but further numerical investigation would help to determine their precise dynamics. As a consequence of nocturnal radiative cooling, the local surface circulation in the vicinity of the Mainland is decoupled (by reduced mixing) from the synoptic circulation aloft and becomes weaker during the night. On the contrary, during daytime, the sea breeze combines with the trade-winds to dramatically enhance the surface circulation (by 25–50%).

A close inspection of the wind pattern between the model and twice-daily observed composites allows us to assess the accuracy of the model parametrization and grid resolution. First, as a consequence of the absence of subgrid-scale roughness parametrization, the spatial extension of orographic blocking appears narrower in the model than in observations. The excessive intensity of drainage flow from the Humboldt slopes may also be related to insufficient surface roughness. Additionally, the absence of air–sea coupling in the model may influence these diurnal processes. Feedback from

the coastal ocean can be expected to affect stability and mixing properties of the MABL (see for example Chelton et al., 2007). In particular, coastal upwelling off the west coast of New Caledonia (Marchesiello et al. and Ganachaud et al., 2010) can be locally enhanced by the H1 corner winds and in turn the cold water anomaly may enhance the sea breeze (and advance the time of onset), but probably reduce the drainage flow process. Similarly, on the east coast, the warm Vauban current may reduce the sea breeze and enhance the land breeze. As for the lagoon circulation (Douillet et al., 2001), the complex wind pattern and its strong diurnal cycle along the shoreline constitutes a key factor to understand the dynamics of the lagoon circulation and its impact on ecosystems (Ouillon et al. and LeBorgne et al., 2010).

## Acknowledgements

We appreciate financial support from the following organizations: the French coastal environment research program PNEC, the New Caledonia research program ZoNéCo, and the IRD. In particular, the PC-cluster used for the WRF simulations was financed through IRD’s scientific computing effort project SPIRALES. We would like to thank the NETLAB developer team, the JPL/NASA team, and the providers of topographic data (DTSI New Caledonia) and meteorological data (Météo-France New Caledonia).

## Appendix A. QuikSCAT 12.5 km processing

### A.1. Refinement

Surface wind data from the SeaWinds Ku-band scatterometer (operating at 13.4 Ghz) onboard QuikSCAT spacecraft have been available since July 1999. Wind speed and direction are inferred from backscatter measurements through the use of a geophysical model function (GMF, Tang et al., 2004). Tang et al. (2004) and Sharma and D’Sa (2008) provide details about the recent resolution improvement operations with QHR12. In the standard processing of the QSCAT data, a 25-km resolution wind product is derived from four ambiguities of  $\sigma^0$ , returned from an egg-shaped antenna footprint with dimensions  $25 \times 35$  km. Using onboard filtering, the egg can be divided into smaller, contiguous “slices” having characteristic dimensions of about  $6 \times 25$  km. Using “slices”, QHR12 provides high-resolution vector winds with the same GMF and ambiguity removal as the standard product. In addition, the land contamination criterion is relaxed in QHR12, including “slices” whose centers are over the water (Tang et al., 2004).

### A.2. Accuracy

The accuracy of wind retrieval is affected by land contamination and the presence of heavy rain. At very low wind speed, the smooth sea surface appears more as a reflector than a scatterer and the uncertainties of wind direction are higher. At high wind speed, the GMF is also limited in its functionality, having a design limit of  $30 \text{ m s}^{-1}$  (Sharma and D’Sa, 2008). Like the standard 25 km resolution product, QHR12 shows lower accuracy for light winds ( $< 3 \text{ m s}^{-1}$ ) and strong winds ( $> 20 \text{ m s}^{-1}$ ). Near the land, lower performances still remain but not significantly worse than the standard product (Tang et al., 2004; Sharma and D’Sa, 2008).

### A.3. Processing of along tracks data

Wind speed and direction are retrieved from QHR12, after excluding rain contaminated Wind Vector Cells (WVCs). We use the direction interval retrieval with threshold nudging (DIRTH) winds and the rain-flag `mp_rain_probability` from the multidimen-

sional histogram (MUDH) rain flagging algorithm. The threshold of 0.2 for the `mp_rain_probability` is used to discard rain contaminated cells; this value is used by Quilfen et al. (2007) who find a good compromise between real rain-contamination and high-wind over-flagging. Data gap and outlier, marked using three times the standard deviation as threshold, are filled with a median filter if the WVC is surrounded with five or more valid WVCs neighbors. Using bilinear interpolation, we map the swath data over a regular grid with  $0.125^\circ$  horizontal spacing. The final dataset includes the neutral equivalent wind from 6244 QuikSCAT tracks occurring in the region at 05-07 LST (sunrise) and 17-19 LST (late afternoon). The period extends from 19-July-1999 to 12-June-2008.

### A.4. Computation of wavenumber spectra

From the QHR12 dataset, we compute the along-track wavenumber of wind speed within the geographical region bounded by  $140^\circ\text{E}$ – $200^\circ\text{E}$  and  $5^\circ\text{N}$ – $45^\circ\text{S}$ , using the methodology detailed in Milliff et al. (2004) and Chelton et al. (2006), and following the limitations of QHR12 addressed in Tang et al. (2004). Across track, there are 152 footprint cells in the QHR12 product. In the far-swath (cells 1–12 and 141–152), there are only two flavors and the two extreme edges never contain enough  $\sigma^0$  measurements to determine wind vectors. The mid-swath (cells 13–65 and 88–140) has the greatest diversity of azimuth and incidence angles, contributing to improvements of measurement quality. In nadir-swath (cells 66–87), wind accuracy decreases as measurement diversity is lower compared to mid-swath. As a consequence of the physical limitation of the instrument’s measurement principle in the far-swath and nadir-swath, these WVCs are excluded from our computation of spectra. Spectra are computed for along-track lines that included at least 270 (3370 km) consecutive no rain or land affected measurements. The individual spectra computed from each of the orbital tracks are then ensemble-averaged over the period 1999–2008.

## Appendix B. Clustering method

To perform the regional surface circulation classification, the dataset QHR12 of daily satellite surface wind measurements for the Austral summer is projected onto its two leading modes of variability and analyzed using a mixture of Gaussian components. We apply the Gaussian Mixture Model (GMM), as detailed by Smyth et al. (1999). The method consists in fitting a linear combination of  $k$  Gaussian density functions to the probability density function (PDF) constructed in the subspace of the two leading principal components. In this method, PCA is conducted only as a means of data reduction. To determine the optimal number of component Gaussian distribution (cluster) that provides the best fit to the data, we use the criterion from Smyth et al. (1999), based on the cross-validated log-likelihood. The classified days resulting from the clustering analysis are used to composite the circulation pattern maps from our three datasets: the twice-daily QHR12 along track, the hourly WRF outputs and the daily NCEP2 reanalysis. In addition, the classification allows us to seek the variability of the dominant regimes of surface circulation and the relationship with the large-scale circulation. The different steps of the clustering method (preprocessing, PCA computing, dimensionality reduction and validation of the optimal number of clusters  $k$ ) are detailed below.

### B.1. Preprocessing

The clustering analysis cannot account for any missing values in the dataset time series, thus a 3-day running mean is applied to the original QHR12 dataset described in Section 2 and Appendix A. As

**Table B1**

Cross-validated log-likelihood and estimated posterior probability as a function of the number of clusters  $k$ , when applying the GMM to 20 random partitions.

	$K = 1$	$K = 2$	$K = 3$	$K = 4$	$K = 5$	$K = 6$
Cross-validated log-likelihood	-2200.8	-2132.3	-2108.9	-2103.3	-2105.7	-2112
Estimated posterior probability	0	0	0	0.92	0.08	0

the study focuses on intra-seasonal variability, the annual and biannual seasonal cycle is removed and a 90-day Lanczos high-pass filter is then applied to remove the inter-annual variability signal. Finally, summer data from 01-November-99 to 30-April-2008 are extracted. The dataset used to train the GMM contains 1632 daily vector wind maps.

PCA is done by using real-vector method, following the method from Ludwig et al. (2004) and Conil and Hall (2006). Each wind component is normalized and weighted by the square root of the cosine of their latitude in order to account for the smaller surface area of grid boxes at higher latitudes. In the real-vector method, the data matrix is formed by appending the meridional wind to the zonal wind anomalies. Fig. 4 shows the percent variances associated with each of the first 15 PCA. Using North's criteria (North et al., 1982), the first two leading modes are distinct and explain 40% of the total variance. The general spatial pattern associated with the first leading mode (27% of the variance) is similar to the dominant ENSO mode in the region (not shown), with a strong positive (negative) anomaly of the SE trade-wind in the vicinity of Vanuatu and New Caledonia during El Niño (La Niña) event. The second leading mode (13% of the variance) exhibits a cyclonic circulation centered around New Caledonia (not shown), but its spatial interpretation is not investigated further.

### B.2. Clustering

To perform the cluster analysis, we use the GMM module written by Nabney I. and Dimitrov A.G from the Matlab toolbox Netlab from (<http://www.ncrg.aston.ac.uk/netlab>). The GMM is applied to the two first leading modes and the cross-validated log-likelihood test is performed with an increasing number of clusters  $k$ , ranking from 1 to 6, following the methodology of Smyth et al. (1999) and Kondrashov et al. (2007). The cross-validation consists of randomly dividing the available data set into two half-data sets, training the model on one of the partitions, and then validating the other. The procedure is repeated 20 times. The estimated posterior probabilities and cross-validated log-likelihoods are tabulated in Table B1.

### B.3. Optimal number of clusters

Fig. 4 shows the result of the PCA conducted on the remote sensed winds to derive the dominant patterns of variability. Using North's criteria (North et al., 1982), the first two leading modes are distinct and explain 40% of the total variance. Next, the values of these two principal components are clustered into homogenous groups using the GMM. Applying Smyth's criterion, we found an optimal number of four clusters to describe the dominant stationary flow regimes represented in the dataset for the nine warm periods of November–April for the years 1999–2008. This number is consistent with the four weather regimes objectively defined by Leroy (2006) with her  $k$ -means method applied on SLP for the same seasonal period with ERA40 dataset. Fig. 5 shows the contour map of the PDF resulting from the linear combination of the four Gaussian density functions. For each Gaussian component, the mean of the Gaussian (cluster centroid) and the 1.5 standard deviation ellipsoid associated with its covariance matrix is super imposed. Each day of satellite wind observation is associated with values of PC1 and PC2 and is also displayed in scatter-plot format in the

phase space spanned by PC1 and PC2. We associate each cluster with a local circulation regime and, following Kondrashov et al. (2007) and Conil and Hall (2006), the wind field observation on any particular day is classified using its distance to the center of the cluster centroid. The extension of the clusters is determined by choosing the covariance ellipsoid with semi-axes equal to 1.5 times the standard deviation in each direction. However, each data point can belong to several clusters, and is thus assigned to a single cluster according to the maximum probability value given by the mixture model (Smyth et al., 1999; Kondrashov et al., 2007). The extension of clusters 2 and 3, shown by their respective covariance ellipse, is larger than for clusters 1 and 4, suggesting that the spatial variability of the surface circulation associated with Regimes 2 and 3 is probably strong, while Regimes 1 and 4 are characterized with more steady circulation conditions. To investigate the robustness of our circulation regime definition, we computed for each regime some statistics applied to the sensed surface wind parameters (speed and direction) for the corresponding days. Means and standard deviation averaged on the regional box corresponding to the innermost WRF domain (see Fig. 6 [162.4E–168.7E; 24.5S–18.6S]) are displayed in Table 3. All regimes exhibit a southeasterly wind direction, but Regime 3 and especially Regime 2 show weak winds with large wind direction variability. Regime 1 is the steadiest, with high surface winds. Our definition of the clusters implies that 12.8% of the days are not classified.

## References

- Atlas Climatique de la Nouvelle-Calédonie, 2007. Météo-France Nouvelle-Calédonie.
- Bauer, M.H., Mayr, G.J., Vergeiner, I., Pichler, H., 2000. Strongly nonlinear flow over and around a three-dimensional mountain as a function of the horizontal aspect ratio. *J. Atmos. Sci.* 57, 3971–3991.
- Burk, S.D., Haack, T., Rogers, L.T., Wagner, L.J., 2003. Island wake dynamics and wake influence on the evaporation duct and radar propagation. *J. Appl. Meteorol.* 42, 349–367.
- Chelton, D.B., Freilich, M.H., Sienkiewicz, J.M., Von Ahn, J.M., 2006. On the use of QuikSCAT scatterometer measurements of surface winds for marine weather prediction. *Mon. Wea. Rev.* 134, 2055–2071.
- Chelton, D.B., Schlax, M.G., Samelson, R.M., 2007. Summertime coupling between sea surface temperature and wind stress in the California current system. *J. Phys. Oceanogr.* 37 (3), 495–517.
- Chen, S., Lin, Y., 2005. Orographic effects on a conditionally unstable flow over an idealized three-dimensional mesoscale mountain. *Meteorol. Atmos. Phys.* 88, 1–21.
- Chèrux, F., Speranza, A., Sutera, A., Tartaglione, N., 2004. Surface winds in the Euro-Mediterranean area: the real resolution of numerical grids. *Ann. Geophys.* 22, 4043–4048.
- Conil, S., Hall, A., 2006. Local regimes of atmospheric variability: a case study of Southern California. *J. Climate* 19, 4308–4325.
- Davidson, K.L., Boyle, P.J., Guest, P.S., 1992. Atmospheric boundary-layer properties affecting wind forecasting in coastal regions. *J. Appl. Meteorol.* 31, 983–994.
- Delcroix, T., Lenormand, O., 1997. ENSO signals in the vicinity of New Caledonia, South Western Pacific. *Oceanological Acta* 20, 481–491.
- Douillet, P., Ouillon, S., Cordier, E., 2001. A numerical model for fine suspended sediment transport in the south-west lagoon of New Caledonia. *Coral Reefs* 20, 361–372.
- Dudhia, J., 1989. Numerical study of convection observed during the winter monsoon experiment using a mesoscale two-dimensional model. *J. Atmos. Sci.* 46, 3077–3107.
- Ganachaud, A., Vega, A., Le Borgne, R., Rodier, M., Maes, C., Marchesiello, P., Lefèvre, J., Soul, F., 2010. Observations of an upwelling impact on water properties and biological activity in New Caledonia. *Mar. Pollut. Bull.* 61, 449–464.
- Hinkle, D.E., Wiersma, W., Jurs, S.G., 2003. *Applied Statistics for the Behavioral Science*, third ed. Houghton Mifflin Company, Boston, USA (5th ed.).
- Hoffman, R.N., Leidner, S.M., 2005. An introduction to the near-real-time QuikSCAT data. *Weather Forecast.* 20, 476–493.

- Hong, S.Y., Dudhia, J., Chen, S.H., 2004. A revised approach to ice microphysical processes for the bulk parameterization of clouds and precipitation. *Mon. Wea. Rev.* 132, 103–120.
- Janjic, Z.I., 1994. The step-mountain eta coordinate model: further developments of the convection, viscous sublayer, and turbulence closure schemes. *Mon. Wea. Rev.* 122, 927–945.
- Jourdain, N.C., Gallée, H., 2010. Influence of the orographic roughness of glacier valleys across the Transantarctic Mountains in an atmospheric regional model. *Clim. Dynam.* (published online). doi: 10.1007/s00382-010-0757-7.
- Kim, Y.J., Doyle, J.D., 2005. Extension of an orographic drag parameterization scheme to incorporate orographic anisotropy and flow blocking. *Q. J. Roy. Meteor. Soc.* 131, 1893–1921.
- Kondrashov, D., Shen, J., Berk, R., D'Andrea, F., Ghil, M., 2007. Predicting weather regime transitions in Northern Hemisphere datasets. *Clim. Dynam.* 29 (5), 535.
- Leborgne, R., Douillet, P., Fichez, R., Torrèton, J.P., 2010. Hydrography and plankton temporal variabilities at different time scales in the southwest lagoon of New Caledonia: a review. *Mar. Pollut. Bull.* 61, 297–308.
- Lefort, T., 2005. Moyenne échéance en Nouvelle-Calédonie. Note interne Météo-France – DIRNC.
- Leopold, L.B., 1949. The interaction of trade wind and sea breeze, Hawaii. *J. Meteor.* 6, 312–320.
- Leroy, A., 2006. Utilisation des prévisions saisonnières en Nouvelle-Calédonie. Note de la DP n°6, Direction de la Climatologie, Météo-France, 169pp.
- Leroy, A., Wheeler, M.C., 2008. Statistical prediction of weekly tropical cyclone activity in the Southern Hemisphere. *Mon. Wea. Rev.* 136, 3637–3654.
- Liang, X.-Z., Xu, M., Zu, J., Kunkel, K.E., Wang, J.X.L., 2005a. Development of the regional climate–weather research and forecasting model (CWRf): treatment of topography. In: Proceedings of the 7th Annual WRF User's Workshop.
- Liang, X.-Z., Xu, M., Zu, J., Choi, H.I.L., Kunkel, K.E., Rontu, L., Geleyn, J.F., Muller, M.D., Joseph, E., Wang, J.X.L., 2005b. Development of the regional climate–weather research and forecasting model (CWRf): treatment of subgrid topography effects. In: Proceedings of the 7th Annual WRF User's Workshop.
- Lin, Y.L., Chiao, S., Wang, T.A., Kaplan, M.L., Weglarz, R.P., 2001. Some common ingredients for heavy orographic rainfall. *Weather Forecast.* 16, 633–660.
- Lott, F., Miller, M.J., 1997. A new subgrid-scale orographic drag parameterization: its formulation and testing. *Q. J. Roy. Meteor. Soc.* 123, 101–128.
- Ludwig, F.L., Horel, J., Whiteman, C.D., 2004. Using EOF analysis to identify important surface wind patterns in mountain valleys. *J. Appl. Meteorol.* 43, 969–983.
- Madden, R.A., Julian, P.R., 1994. Observations of the 40–50 day tropical oscillation: a review. *Mon. Wea. Rev.* 122, 814–837.
- Marchesiello, P., Lefèvre, J., Vega, A., Couvelard, X., Menkes, C., Ganachaud, A., 2010. Coastal upwelling, circulation and heat balance around New Caledonia's barrier reef. *Mar. Pollut. Bull.* 61, 432–448.
- Milliff, R.F., Morzel, J., Chelton, D.B., Freilich, M.H., 2004. Wind stress curl and wind stress divergence biases from rain effects on QSCAT surface wind retrievals. *J. Atmos. Oceanic Technol.* 21, 1216–1231.
- Mlawer, E.J., Taubman, S.J., Brown, P.D., Iacono, M.J., Clough, S.A., 1997. Radiative transfer for inhomogeneous atmospheres: RRTM, a validated correlated-k model for the longwave. *J. Geophys. Res.* 102, 16663–16682.
- Moore, G.W.K., Renfrew, I.A., 2005. Tip jets and barrier winds: a QuikSCAT climatology of high wind speed events around Greenland. *J. Climate* 18, 3713–3725.
- Mostovoy, G.V., Fitzpatrick, P.J., Li, Y., 2005. Regional accuracy of QuikSCAT gridded winds. *Int. J. Remote Sens.* 26, 4117–4136.
- Noh, Y., Cheon, W.G., Hong, S.Y., Raasch, S., 2003. Improvement of the K-profile model for the planetary boundary layer based on large eddy simulation data. *Bound.-Lay. Meteorol.* 107, 401–427.
- North, G.R., Bell, T.L., Cahalan, R.F., Moeng, F.J., 1982. Sampling errors in the estimation of empirical orthogonal functions. *Mon. Wea. Rev.* 110, 699–706.
- Ólafsson, H., Bougeault, P., 1997. The effect of rotation and surface friction on orographic drag. *J. Atmos. Sci.* 54, 193–210.
- Quillon, S., Douillet, P., Lefebvre, J.P., Le Gendre, R., Bonneton, P., Jouon, A., Fernandez, J.M., Chevillon, C., Magand, O., Lefèvre, J., Le Hir, P., Dumas, F., Marchesiello, P., Andréfouët, S., Panché, J.Y., Fichez, R., 2010. Circulation and suspended sediment transport in a coral reef lagoon: the southwest lagoon of New Caledonia. *Mar. Pollut. Bull.* 61, 269–296.
- Overland, J.E., Bond, N.A., 1995. Observations and scale analysis of coastal wind jets. *Mon. Wea. Rev.* 123, 2934–2941.
- Petersen, G.N., Kristjansson, J.E., Olafsson, H., 2005. The effect of upstream wind direction on atmospheric flow in the vicinity of a large mountain. *Q. J. Roy. Meteorol. Soc.* 131, 1113–1128.
- Pierrehumbert, R., Wyman, B., 1985. Upstream effects of mesoscale mountains. *J. Atmos. Sci.* 42, 977–1003.
- Quilfen, Y., Prigent, C., Chapron, B., Mouche, A., Houti, N., 2007. The potential of QuikSCAT and WindSat observations for the estimation of sea surface wind vector under severe weather conditions. *J. Geophys. Res.* 112, C09023.
- Reinecke, P.A., Durran, D.R., 2008. Estimating topographic blocking using a Froude number when the static stability is nonuniform. *J. Atmos. Sci.* 65, 1035–1048.
- Reynolds, R.W., Smith, T.M., 1994. Improved global sea surface temperature analyses. *J. Climate* 7, 929–948.
- Robertson, A.W., Kirshner, S., Smyth, P., Charles, S.P., Bates, B.C., 2006. Subseasonal-to-interdecadal variability of the Australian over North Queensland. *Q. J. Roy. Meteor. Soc.* 132, 519–542.
- Sharma, N., D'Sa, E.J., 2008. Assessment and analysis of QuikSCAT vector wind products for the Gulf of Mexico: a long-term and hurricane analysis. *Sensors* 8, 1927–1949.
- Sinclair, M.R., 1996. A climatology of anticyclones and blocking for the Southern Hemisphere. *Mon. Wea. Rev.* 124, 245–263.
- Skamarock, W.C., 2004. Evaluating mesoscale NWP models using kinetic energy spectra. *Mon. Wea. Rev.* 132, 3019–3032.
- Skamarock, W.C., Klemp, J.B., Dudhia, J., Gill, D.O., Barker, D.M., Wang, W., Powers, J.G., 2005. A Description of the Advanced Research WRF Version 2. NCAR Technical Note.
- Smith, R.B., 1989. Hydrostatic airflow over mountains. *Adv. Geophys.* 31, 59–81.
- Smith, R.B., Gleason, A.C., Gluhosky, P.A., Grubišić, V., 1997. The wake of St. Vincent. *J. Atmos. Sci.* 54, 606–623.
- Smyth, P., Ide, K., Ghil, M., 1999. Multiple regimes in Northern Hemisphere height via mixture model clustering. *J. Atmos. Sci.* 56, 3704.
- Soler, M.R., Infante, C., Buenestado, P., Mahrt, L., 2002. Observations of nocturnal drainage flow in a shallow gully. *Bound.-Lay. Meteorol.* 105 (2), 253–273.
- Tang, W., Liu, W.T., Stiles, B.W., 2004. Evaluation of high-resolution ocean surface vector winds measured by QuikSCAT scatterometer in coastal regions. *IEEE* 42 (8), 1762–1769.
- Trenberth, K.E., Large, W.G., Olson, J.G., 1990. The mean annual cycle in global ocean wind stress. *J. Phys. Oceanogr.* 20, 1742–1760.
- Vautard, R., Mo, K., Ghil, M., 1990. Statistical significance test for transition matrices of atmospheric Markov chains. *J. Atmos. Sci.* 47, 1926–1931.
- Vincent, D., 1994. The South Pacific convergence zone: a review. *Mon. Wea. Rev.* 122, 1949–1969.
- Vosper, S.B., Brown, A.R., 2007. The effect of small-scale hills on orographic drag. *Q. J. Roy. Meteorol. Soc.* 133, 1345–1352.
- Wheeler, M.C., Hendon, H.H., 2004. An all-season real-time multivariate MJO index: development of an index for monitoring and prediction. *Mon. Wea. Rev.* 132, 1917–1932.
- Willmott, C.J., 1981. On the validation of models. *Phys. Geogr.* 2, 184–194.
- Xi, X., 2007. A Comparison of Two Land Surface Schemes Coupled in the Weather Research and Forecast Model. 2007 Fall EAS6140 'Thermodynamics of Atmospheres and Oceans' Term Paper. Georgia Institute of Technology, Atlanta, USA.
- Yang, Y., Chen, Y.L., 2008. Effects of terrain heights and sizes on island-scale circulations and rainfall for the island of Hawaii during HaRP. *Mon. Wea. Rev.* 136, 120–146.